UNIVERSITÀ DEGLI STUDI DI PADOVA
DIPARTIMENTO DI INGEGNERIA DELL'INFORMAZIONE
TESI DI LAUREA

HIGH-INDEX CONTRAST GRATING REFLECTORS FOR WAVEFRONT ENGINEERING

RELATORE: Ch.mo Prof. Marco Santagiustina

LAUREANDO: *Luca Carletti*

Padova, 17 Ottobre 2011

Abstract

High-index contrast grating mirrors providing wave front control of the transmitted light as well as high reflectivity over a broad bandwidth are suggested and both numerically and experimentally investigated. General design rules to engineer these structures for different applications are derived. Such grating mirrors would have a significant impact on low cost laser fabrication, since a more efficient integration of optoelectronic modules can be achieved by avoiding expensive external lens systems.

Contents

1 Introduction **1**

1.1 Diffraction Gratings 4

1.2 High-index Contrast Gratings 7

2 Numerical Methods **11**

2.1 Rigorous Coupled-Wave Analysis 11

2.1.1 Numerical convergence of implemented methods 14

2.2 Finite Element Method 15

3 Phase Front Engineering **21**

3.1 Phase control with high-index contrast gratings 21

3.2 Periodic high-index contrast gratings 23

3.3 Non-periodic high-index contrast gratings 26

3.3.1 Beam focusing 27

3.3.2 Beam steering 30

4 Fabrication Process **33**

4.1 Electron beam Lithography 33

4.2 Dry Etching 35

5 Characterization **39**

5.1 Experimental Setup 39

5.1.1 Alignment 40

5.2 Beam Focusing 41

5.3 Beam Steering 42

6 Conclusion **45**

A Articles Written From This Thesis **47**

Bibliography **53**

Chapter 1

Introduction

The term diffraction, from the Latin "diffringere" that means "to break into pieces", was first coined by Francesco Maria Grimaldi in 1665. From then on, diffraction gratings have been thoroughly studied by physicists and engineers. Nowadays they are broadly used in optical devices as for example in spectrometers, lasers, wavelength division multiplexing systems or optical pulse compressing devices. Their extensive use in optical components has been attractive because of their particular optical properties gained by diffraction of light caused by the structure. For instance, gratings are used to provide high reflectivity mirrors with low losses that are essential for laser systems. An example of these gratings are the well known Bragg gratings.

The considerable development over the last decade of new modeling tools and fabrication technologies has led to the possibility of investigating a new type of gratings with sub-wavelength periodicity called high-index contrast gratings (HCGs). These gratings have drawn a lot of attention due to their capability of providing very high reflectivity over a broad bandwidth [1], with a simple and compact structure. HGCs can be used to replace conventional Bragg gratings, as applied e.g. in vertical-cavity surface-emitting lasers (VCSELs), enabling the engineering of a new set of interesting properties beneficial for different applications. These include simpler epitaxial structure [2], high differential efficiency [2], strong single-transverse-mode operation [3], broad wavelength tunability [4], and light emission into an in-plane silicon photonics chip [5]. Another interesting property of HCGs is that the phase of the reflected beam can be engineered by modifying the grating design. Recent work [6] has demonstrated the ability to

focus the reflected beam. For integration into VCSELs, wave front control of the transmitted beam is more advantageous.

In optoelectronic modules production, typically 60% to 90% of the final cost resides in the packaging process. Therefore cost-effective solutions are necessary to achieve affordable fiber-to-the-home optical communication systems deployment. For example, a source of cost is the need to focus the output beam by the use of external lenses in order to optimize the output coupling efficiency. In the approach of this work, a Si-hybrid structure design is employed to integrate the functionality of these lenses in the VCSEL itself. Employing an HCG mirror with sub-wavelength structuring, the phase front of the transmitted wave can thus be engineered. This is achievable by locally modifying the grating periodicity or its duty cycle, i.e. the fraction of high index material in one grating period. With this method quadratic or linearly varying phase profiles for the transmitted beam are obtained without the need of additional components. For example, as illustrated in Fig. 1.1(a), having a focused output beam could facilitate the light collection from a VCSEL chip to an optical fiber. Another application might be light collection from multiple VSCEL chips to a single optical fiber by directly steering the output light of each VCSEL chip as show in Fig. 1.1(c). Otherwise, a lens for these beam collections would be needed (Figs. 1.1(b) and 1.1(d)). As depicted in Fig. 1.1(e), dynamic beam steering would also be possible if the refractive indices of constituting gratings in a HCG are controlled by using the electro-optic effect or the free-carrier plasma effect. The analog feature could be obtained for beam focusing by applying the same principle. These novel functionalities will be able to considerably reduce the lens/optics packaging cost and provide design flexibilities in the packaging and free-space optical interconnects.

In this work, the fundamental ability of an HCG to manipulate the phase front of a transmitted light beam is investigated and useful design rules for the realization of practical structures are formulated. Based on these rules, HCG structures are fabricated and experimentally demonstrated to have either focusing or beam steering ability, while maintaining a high reflectivity. Such structures are promising for replacing the output mirror in VCSELs. The manuscript is organized as follows. In the following introduction a brief review of the physical principles of diffraction gratings is provided. High-index contrast gratings are presented emphasizing differences and similarities with respect to ordinary grat-

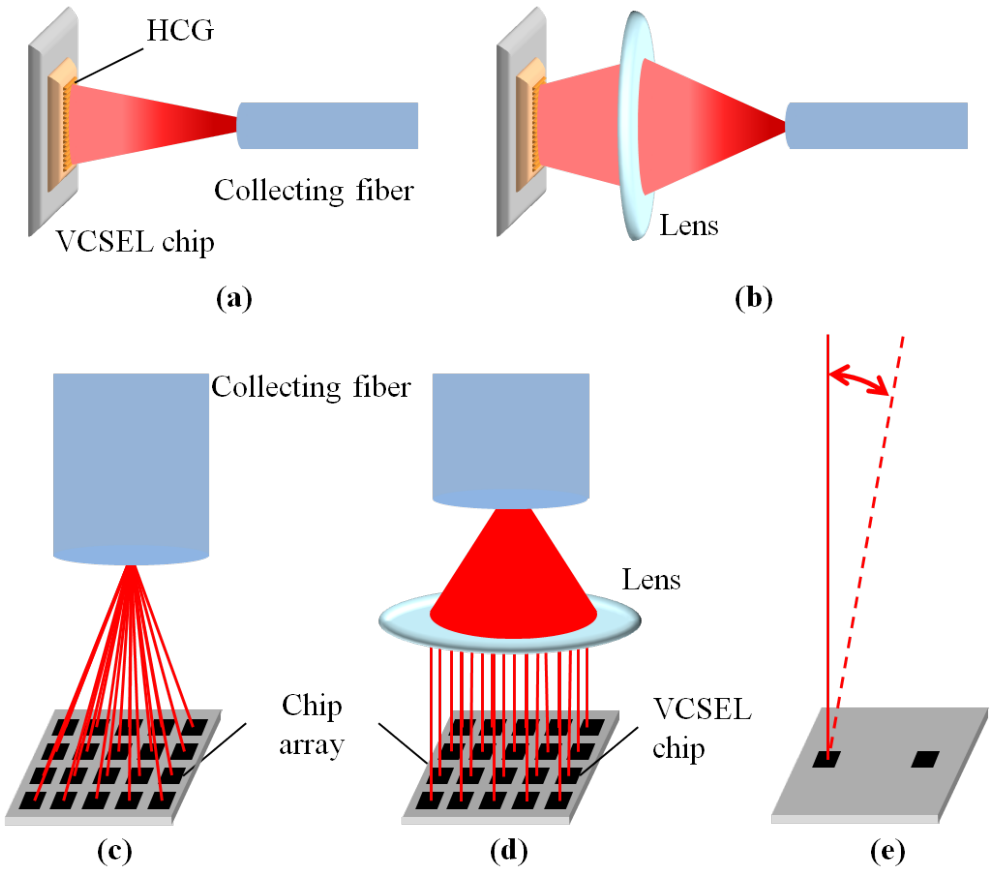

Figure 1.1: In (a) light coupling from a VCSEL chip to an optical fiber by employing a HCG with focusing abilities is shown. In (c) light coupling from multiple VCSEL chips to an optical fiber by using the HCGs is shown. In (b) and (d) light coupling is performed by using a lens. (e) Beam propagation angle can be dynamically steered between the solid and dashed lines.

ings. In Chapter 2, the simulation methods employed to determine the properties of periodic and non-periodic HCG structures are briefly described. In Chapter 3, the HCG design issues as well as numerical simulation results are discussed. The procedure to design a HCG structure with a certain phase profile that complies with additional application requirements is explained. In Chapter 4, the fabrication process to produce the HCGs of this project is described. In Chapter 5, the experimental characterization results presented demonstrate the wave-front manipulation ability of the designed HCGs. The theoretical rules are compared with the measurements and good agreement is found.

1.1 Diffraction Gratings

A diffraction grating is a periodic structure made of dielectrics with different refractive indices. Depending on the spatial direction of the periodicity, gratings can be one-, two- or three-dimensional structures. Due to the particular arrangement of the materials, the phase and the amplitude of an incident beam is modulated by the grating. The light that goes through this structure is called diffracted light. The periodicity of the structure and the refractive index difference determine the properties of the diffracted wave; The reflectivity at certain wavelengths may be tailored by altering the grating parameters. An example of a one-dimensional grating is shown in Fig. 1.2. The structure is periodic in the x-axis direction with grating periodicity, Λ. A plane wave is assumed to be incident on the grating with an angle, θ_i, relative to the normal direction to the grating plane, $\hat{n}$. Following the Huygens-Fresnel principle, light reflected from every different grating groove will act as a source in the reflected wave front. These source points have different phases due to different traversed distances and, thus, an interference pattern is seen in the scattered light. The type of interference, either constructive or destructive, depends on the phase difference between the source points. In general, to have constructive interference the path difference between points of the same wave front has to be an integer multiple of the wavelength of the light, λ. This condition is expressed by

$$\sin\theta_{d,m} = \sin\theta_i + m\frac{\lambda}{\Lambda} \qquad \text{m}=0,\pm1,\pm2,\ldots \tag{1.1}$$

where $\theta_{d,m}$ is the angle formed between the $m-$th order diffracted mode direction and the normal direction $\hat{n}$, and θ_i is the incident angle as depicted in Fig. 1.2. A similar result is obtained for the transmitted light. A more general expression is obtained by introducing the wave number $k = 2\pi/\lambda$ and by defining the grating wave number $K = 2\pi/\Lambda$:

$$k_{x,m} = k_{x,i} + mK \qquad \text{m}=0,\pm1,\pm2,\ldots \tag{1.2}$$

where the subscript x is for the x component of the wave vector, $k_x = k\sin\theta_{d,m}$.

From Eq.(1.1), assuming normal incidence, it is observed that a sufficient and necessary condition for the diffracted mode to exist is given by

$$|\sin\theta_{d,m}| < 1 \qquad \Leftrightarrow \qquad \left|m\frac{\lambda}{\Lambda}\right| = \left|m\frac{K}{k}\right| < 1. \tag{1.3}$$

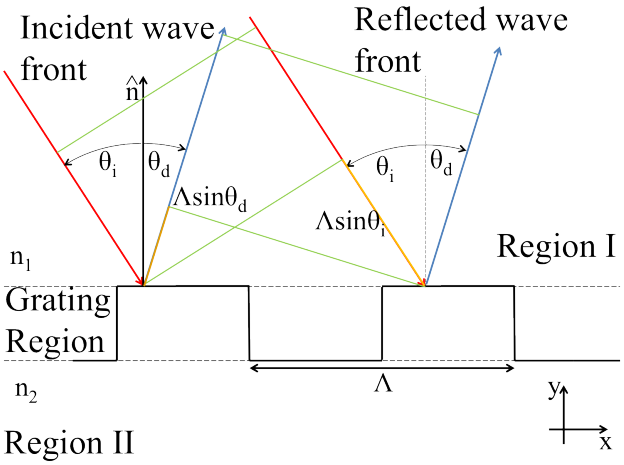

Figure 1.2: Example of a one-dimensional grating. In the grating region the refractive index is periodic with periodicity Λ as a function of the x-axis coordinate and it varies from n_1 to n_2. At the reflected wavefront the difference in propagated distance determines the interference type.

Eq.(1.3) determines the maximum diffraction order mode of the scattered light. In particular, this depends on the ratio between the wavelength and the grating periodicity.

A common and extensively employed grating in photonic devices is the Bragg grating. In Fig. 1.3(a) a one-dimensional Bragg grating is illustrated. This is characterized by a periodic alternation of two layers of different dielectrics. The spectral properties of this grating are described by Bragg's law that is deduced following the same basic principle that led to Eq.(1.1):

$$m\frac{\lambda_B}{\bar{n}} = 2\Lambda \sin\theta_i \tag{1.4}$$

where m is an integer, λ_B is the Bragg wavelength and $\bar{n}$ is the average refractive index in one grating period Λ:

$$\bar{n} = \frac{n_1 L_1 + n_2 L_2}{\Lambda} \tag{1.5}$$

where n_1, L_1 and n_2, L_2 are the refractive indices and lengths of the two dielectrics of the grating.

The spectrum of different Bragg reflectors is reported in Fig. 1.3(b). It is seen that there is one wavelength at the center of the high reflectivity bandwidth for which the reflection is always maximum. This wavelength is the Bragg wavelength, λ_B. An important observation is the dependency of the spectrum on the

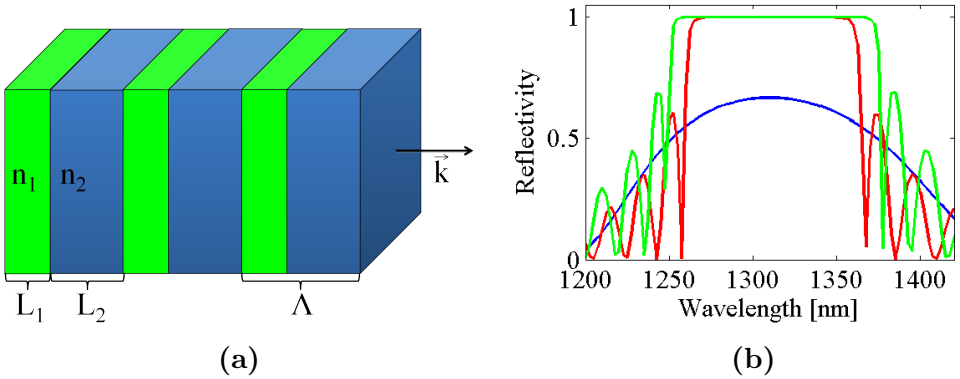

Figure 1.3: Example of a one-dimensional Bragg grating. In the grating region the refractive index varies periodically between n_1 and n_2 with periodicity Λ as a function of the x-axis coordinate. In (b) the reflectivity spectra of different Bragg gratings with $\lambda_B = 1310$ nm are shown. The blue and red curves represent two gratings with $\Delta n = 0.36$ and 30 and 50 periods Λ respectively. The green curve is for a grating with 50 periods, but $\Delta n = 0.45$.

number of grating periods and on the refractive index difference Δn. For a fixed Δn, the high reflectivity bandwidth of the grating as well as the reflectivity at λ_B increase by increasing the number of periods, as seen by comparing the blue and red spectra in Fig. 1.3(b). This occurs because, while increasing the number of periods, more and more contributions from partial internal reflections within the structure interfere to form the diffracted beam. On the other hand, if the number of periods is constant but Δn is increased, the high reflection bandwidth broadens as seen by comparing the red and green spectra of Fig. 1.3(b). A figure of merit for these phenomena is the diffraction efficiency that is defined as the ratio of the diffracted light intensity, of a given diffraction order, to the incident light intensity. For example, if Δn is small, the reflectivity given by the internal interfaces will be small and thus the intensity of the diffracted beam will be lower than the case with a large Δn. Thus, for the same number of periods, the diffraction efficiency of a grating increases with an higher Δn. This implies that, to obtain a certain reflection bandwidth, if Δn is larger the diffraction efficiency is higher and fewer grating periods will be necessary, allowing to have a smaller structure. Therefore, for photonic devices application, the limitation of Bragg gratings is twofold. From one side the refractive index difference between the two materials of the grating cannot be very high because of lattice match constraints.

If the lattice mismatch is large, the molecular structure is strained and defect points appear, prejudging the device functionality [7]. On the other hand, poor refractive index differences decrease the diffraction efficiency and many periods are required to achieve a high reflectivity over a broad band. Because of this, Bragg reflectors used, for example in VCSEL structures, are usually made of 40-50 periods leading to a total thickness that is around 5-6 μm. This increases the complexity of the epitaxial growth and impoverishes the thermal relaxation properties of the device. On the other side, the new type of diffraction gratings called high-index contrast gratings (HCGs), discussed in the next section, provide many advantages compared to Bragg reflectors. In these novel structures a high refractive index difference, Δn, is achieved with very small sizes, e.g 0.5-1 µm, and approximately 1000-times smaller mass than Bragg reflectors. This large refractive index variation within the structure confers to HCGs many physical properties that are beneficial for various applications in photonics, as e.g. broad high reflectivity bandwidth, polarization selectivity or single-transverse mode operation.

1.2 High-index Contrast Gratings

HCGs are gratings with a sub-wavelength periodic patterning fabricated with materials exhibiting a large refractive index difference. For instance, these structures may be made of Si and air, as considered in this work, or InP and air. The type of gratings analyzed is shown in Fig. 1.4. Between the HCG layer and the active (InP-based) material layer of a VCSEL, a low refractive index SiO_2 gap layer is incorporated. The structural parameters depicted in Fig. 1.4 determine the transmission and reflection properties of the grating. These parameters are grating thickness, t_g, grating periodicity, Λ, duty cycle, DC, i.e. the fraction of high refractive index material in one grating period, and low-refractive index material thickness, t_l. The refractive indices of the materials used are also important to determine the spectral response and they are 3.47 for Si, 1.47 for SiO_2 and 3.2 for InP. An alternative design might be an InP grating with an air [2] or oxide [3] gap layer below.

In HCGs, reflection and transmission are not caused by diffraction as the only diffraction order found in the transmitted or reflected beam is the 0th. In

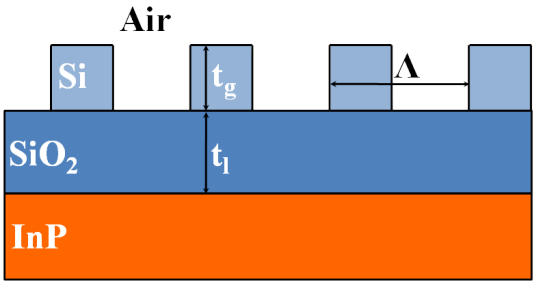

Figure 1.4: Example of a one-dimensional HCG implemented in Si over a SiO_2 low-index layer. The substrate material is InP and the output material, at the transmission side, is air.

fact, from Eq.(1.3), the ratio λ/Λ is bigger than one for sub-wavelength grating periodicity. In these structures, reflection and transmission are the result of coupling of the radiative optical mode to the photonic bandgap (PBG) modes of the photonic crystal structure constituted by the HCG [8]. High order diffracted modes are diffracted at grazing angle. These modes can couple to PBG modes of the structure if the parallel components of the wave vectors coincide. Therefore, the waveguided mode is a lossy mode, because it can couple to a radiated mode. This conditions on the wave vector may be fulfilled in the region above the light line of the dispersion characteristic of the HCG structure.

The characteristic time of the coupling between radiated and waveguided modes is the photon lifetime, τ_c, defined as the average time that photons spend in the structure before reemission into free-space. The high reflectivity bandwidth is inversely proportional to the photon lifetime, i.e. $\delta\omega \propto 1/\tau_c$ where $\delta\omega$ is the high reflectivity bandwidth. Another parameter to characterize the reflection is the reflection delay time, τ_d, that is defined as the time taken for incident light to be reflected from the HCG. This quantity is directly related to τ_c; If photons stay longer in the structure, light reflection will take a longer time.

Based on the properties of the reflection delay time, τ_d, and photon lifetime, τ_c, HCGs can be categorized into two different categories [5]. The first type are slow HCGs. By observing the dispersion diagram of the photonic crystal, for wave vectors lying on the x axis ($\beta = 0$) a PBG mode is found at the resonant frequency. Therefore the waveguided modes involved are modes propagating in the horizontal direction (Fig. 1.5(a)). The photon lifetime, τ_c, is long because a small portion of photons is incident at the HCG-air interfaces. Thus, due to a

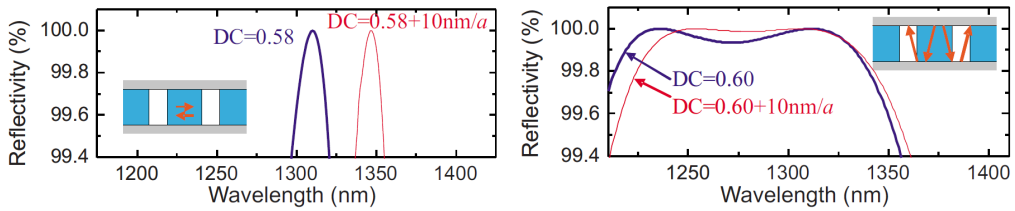

Figure 1.5: Reflectivity spectra of a slow in (a) and fast in (b) HCG. The slow HCG has Λ=730.5 nm, t_g=250 nm, and DC=0.58 while the fast HCG has Λ=515 nm, thickness, t_g=355 nm, and DC=0.6. The red thin curves show the result of increasing the DC by 10 nm/Λ. Reproduced from [5]

long τ_c, the reflection delay time, τ_d, is long. The second type are fast HCGs. The waveguided modes involved in the reflection mechanism are vertically-propagating modes (Fig. 1.5(b)). This is deduced by the fact that no PBG modes are found at the resonant frequency in the photonic crystal dispersion diagram for $\beta = 0$. The photon lifetime, τ_c, is small due to frequent scattering of photons at the HCG-air interface, and therefore τ_d is short. The two different types of HCG can be distinguished from the reflection spectrum of Fig. 1.5. Due to short τ_c, fast HCGs feature a broader high reflectivity bands, $\delta\omega$, than slow HCGs. Two close resonance peaks may also merge and result in a broader high reflectivity bandwidth. Due to this broad resonance, fast HCGs provide higher fabrication tolerance than slow HCGs as seen by comparing the differences between the blue and the red curves of Figs. 1.5(a) and 1.5(b).

Chapter 2

Numerical Methods

Two different numerical methods have been used to analyze the reflection and transmission spectra of high-index contrast grating structures. This chapter provides an introduction to these methods. To confirm the validity of the implementations of the methods used, the results obtained from numerical simulations are compared to results found in the literature. Furthermore, the choice of the method employed for modeling each different structure is explained.

2.1 Rigorous Coupled-Wave Analysis

Rigorous coupled-wave analysis (RCWA) is used to analyze light propagation through a structure with a periodically varying refractive index [9]. This method is often used to investigate planar gratings because it allows to analyze the spectrum of different structures in a short amount of time and with a good accuracy. Furthermore, the coupled-wave approach gives superior physical insight into the diffraction phenomena and frequently yields simple analytical results. In this method Maxwell's equations are solved exactly for light diffraction by grating structures. Reflectance and transmittance are found by solving the boundary conditions of the specific problem.

Considering the structure in Fig. 2.1(a), it is observed that the relative permittivity, i.e. $\varepsilon_r = n^2$, in the grating region is periodic in the x-axis direction and thus it may be expressed using its Fourier series:

$$\varepsilon_r(x) = \sum_{k=-\infty}^{+\infty} \varepsilon_k \exp\left(j\frac{2\pi k x}{\Lambda}\right) \tag{2.1}$$

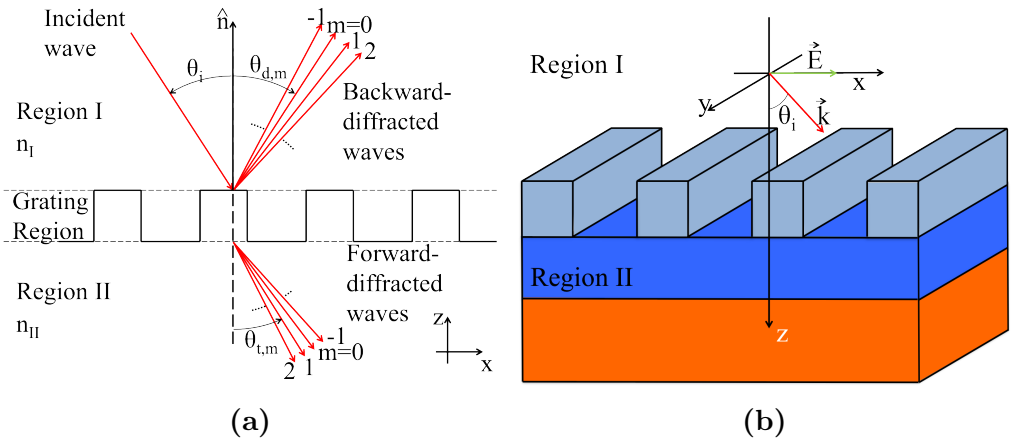

Figure 2.1: (a) one dimensional grating, which is periodic in the x-axis direction. The incident wave is backward diffracted in Region I and forward diffracted in Region II through the grating. A 3-dimensional illustration of the grating is shown in (b), where the polarization of an incident TM field is also indicated.

where ε_k is the k-th spatial Fourier harmonic and Λ is the grating period.

The polarization of the incident light is assumed to be transverse-magnetic (TM) which corresponds to the case depicted in Fig. 2.1(b). The electric field vector is orthogonal to the grating grooves direction, i.e. orthogonal to the y-axis direction in the example. Transverse-electric (TE) polarization is defined with the electric field vector parallel to the grating grooves direction. The analysis for the TE case proceeds similarly to the TM case. For the incident field being TM polarized, the magnetic field is normal to the plane of incidence and may be written as

$$H_{inc,y} = \exp\left[-jk_0 n_I (x \sin\theta_i + z \cos\theta_i)\right] \tag{2.2}$$

where $k_0 = 2\pi/\lambda_0$ is the wavenumber, relative to the λ_0 free space wavelength, n_I is the refractive index in region I and θ_i is the angle of incidence. The incident field will be diffracted in many modes from the grating as described in Eq.(1.1). The total field in region I may be seen as a superposition of the incident field and the backward diffracted waves. Likewise, the field in region II may be interpreted as the superposition of all the forward diffracted waves. In this picture, depicted in Fig. 2.1(a), the magnetic field in regions I and II may be written as [10]

$$H_{I,y} = H_{inc,y} + \sum_i R_i \exp\left[-j(k_{xi}x - k_{I,zi}z)\right] \tag{2.3}$$

$$H_{II,y} = \sum_i T_i \exp\left\{-j\left[(k_{xi}x - k_{II,zi}(z-d)\right]\right\}. \tag{2.4}$$

R_i and T_i are the reflection and transmission coefficients for the i-th order diffracted mode and the other parameters are defined for any mode, i, as

$$k_{x,i} = k_0[n_I \sin\theta - i(\lambda_0/\Lambda)] \tag{2.5}$$

$$k_{l,zi} = \begin{cases} k_0[n_l^2 - (k_{xi}/k_0)^2]^{1/2}, & \text{if } k_{xi}/k_0 < n_l \\ -jk_0[(k_{xi}/k_0)^2 - n_l^2]^{1/2}, & \text{if } k_{xi}/k_0 > n_l \end{cases} \qquad l = I, II \tag{2.6}$$

The electric field is obtained from Maxwell's equations once the magnetic field is known:

$$\mathbf{E} = \left(\frac{-j}{\omega\varepsilon_0 n^2}\right) \nabla \times \mathbf{H}. \tag{2.7}$$

The tangential magnetic (y-axis component) and electric (x-axis component) fields in the grating region are expressed using the Fourier expansion:

$$H_{g,y} = \sum_{i=-\infty}^{+\infty} U_{y,i}(z) \exp(-jk_{xi}x) \tag{2.8}$$

$$E_{g,x} = j\left(\frac{\mu_0}{\varepsilon_0}\right)^{1/2} \sum_{i=-\infty}^{+\infty} S_{x,i}(z) \exp(-jk_{xi}x) \tag{2.9}$$

where $U_{y,i}(z)$ and $S_{x,i}(z)$ are the amplitudes of the $i-$th space harmonic of the solution of the Maxwell's equations in the grating region.

By inserting Eqs. (2.8) and (2.9) into the Maxwell's equations for the grating region, a system of coupled-wave equations is established. This system, called state-equation, can be rewritten in a matrix formulation that ensures a stable and efficient numerical implementation [11], [12]. The reflection and transmission coefficients are found from the solution of the state-equation by applying the boundary conditions. These require continuity of the tangential components of the electric and magnetic fields at the interfaces between the different regions. It is observed that the computational load of the numerical problem is proportional to the number of harmonics, n, retained in the Fourier expansions of Eq. (2.8). In fact, for each harmonic component, there are two boundary conditions leading to a set of $2n$ equations that can be rewritten in an $n \times n$ matrix. To solve the system retaining an higher number of modes, n, produces more accurate results but also increases the computational load.

2.1.1 Numerical convergence of implemented methods

In this project, two different implementations of the RCWA method have been tested. The oldest one is called rigorous optical diffraction software (RODIS) [13] and it has been already used to obtain previous results like [4]. This implementation is based on the program language Python and thus integration with Matlab may result cumbersome. A newer RCWA implementation is offered by ricwaa 1.0.2 [14] and it is developed on a complete Matlab platform. To compare these two implementations, convergence studies and comparison with results found in the literature have been performed.

Efficient convergence of the RCWA method is ensured by the matrix formulation suggested in [12]. To further improve the convergence, it is useful to adopt, rather than the ideal square wave profile, a super-gaussian refractive index profile:

$$n(x) = n_1 + (n_2 - n_1)\exp(-(x/w)^{2m}) \tag{2.10}$$

where n_1 and n_2 are the lowest and highest refractive indices in the grating, x is the x-axis coordinate, w is the width of the grating grooves and m is the order of the super-gaussian approximation. This feature was not originally included in the ricwaa 1.0.2 distribution and thus it has been developed in this work. The two refractive index distributions are compared in Fig. 2.2(a). It is noted that the higher the order m, the closer the super-gaussian approximation is to the squared profile function. The super-gaussian distribution is a more a physically realistic distribution than the step function and, due to continuity of its derivative, convergence of its Fourier series is ensured. In Fig. 2.2(b) the convergence behavior of the different RCWA implementations is shown. In ricwaa 1.0.2 the results employing both the step and super-gaussian refractive index distributions are compared with the results obtained with RODIS. It is seen that convergence, in terms of number of modes retained, m, in RODIS is faster than in ricwaa 1.0.2.

To assess the correctness of the results given by the different implementations, the reflection spectrum of the HCG reported in [4] is chosen as reference. In Fig. 2.2(c) a good agreement between RODIS and ricwaa 1.0.2 simulations with the literature results is seen.

In conclusion, the results from both RCWA implementations, RODIS and ricwaa 1.0.2, are very close to the results reported in the literature but the need of using a higher number of modes, m, in ricwaa 1.0.2 than in RODIS increases

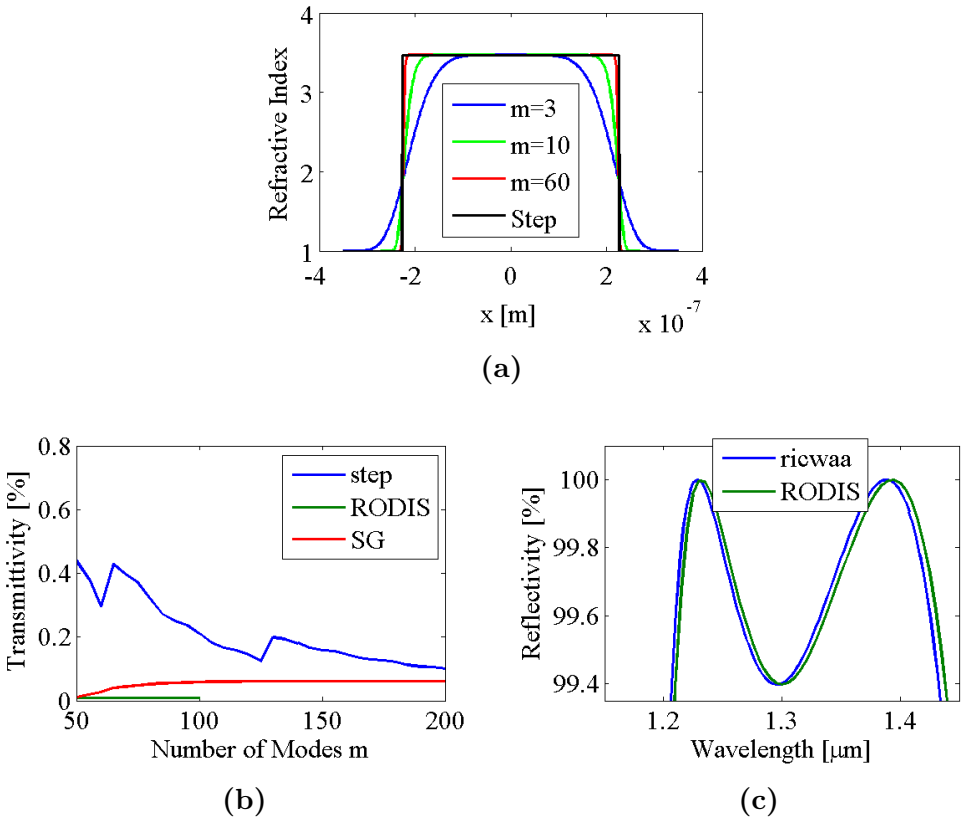

Figure 2.2: (a) Comparison of step refractive index distributions and super-gaussian profile with order m being 3, 10 and 60. The super-gaussian approximation is employed instead of the step function in ricwaa 1.0.2 to improve the convergence. In (b) the convergence of the different methods as a function of the number of modes retained is shown. SG and Step denote ricwaa 1.0.2 results using super-gaussian and step index distributions respectively. In (c) the results obtained by simulation of the HCG in [4] are compared to ricwaa 1.0.2, employing super-gaussian approximation, and RODIS.

the computational load and thus the simulation time. For this reason the implementation of RCWA chosen for this project is RODIS.

2.2 Finite Element Method

In the RCWA method, the solutions used in Eqs (2.3),(2.4) and (2.8) were derived using the Floquet theorem, which is valid only for infinite periodic structures [15]. In this work, to achieve wave-front control, non-periodic structures have to be investigated. A simulation tool not limited by structural constraints is, for instance, finite element method (FEM) [16]. The numerical simulations performed

with this method have been obtained using the commercial software *COMSOL*, which implements FEM.

The FEM is a numerical technique to solve partial differential equations using numerically stable approximations. The basic idea is to discretize continuous functions and operators to numerically compute the solution in a manner that reduces the errors or numerical artifacts. The simulation domain is sampled using a mesh. A straightforward example of an important simulation parameter to chose is the domain sampling distance or mesh elements distance. In optical problems, wave propagation is characterized by the wavelength of light, λ. Thus, it is found that a spacing between mesh elements not larger than a fraction of the wavelength is adequate to avoid numerical artifacts and obtain accurate results. An optimum choice that minimizes the computational load and gives results with good accuracy is $\lambda/10$. An example of a portion of a generated mesh is shown in Fig. 2.3(a). An extensive and complete explanation of the discretization techniques adopted in FEM is out of the scope of this thesis. For more details about this method many books and articles can be consulted, e.g. [17] and [18]. In the following, some important aspects related to the numerical simulations performed are discussed.

The boundary conditions are crucial to obtain meaningful results that describe the physical properties of the real system. From Maxwell's equations, the fields at an interface between two different materials are related through

$$\hat{n}_2 \times (\mathbf{E_1} - \mathbf{E_2}) = 0 \tag{2.11}$$

$$\hat{n}_2 \times (\mathbf{H_1} - \mathbf{H_2}) = \mathbf{J_s} \tag{2.12}$$

$$\hat{n}_2 \cdot (\mathbf{D_1} - \mathbf{D_2}) = \rho_s \tag{2.13}$$

$$\hat{n}_2 \cdot (\mathbf{B_1} - \mathbf{B_2}) = 0 \tag{2.14}$$

where $\hat{n}_2$ is the outward normal from medium 2 and ρ_s and $\mathbf{J_s}$ are surface charge density and surface current density, respectively. Eqs.(2.11)-(2.12) establish a relation between the tangential components of electric, $\mathbf{E}$, and magnetic, $\mathbf{H}$, fields in the two media at the boundary. Likewise, Eqs.(2.13)-(2.14) relate the perpendicular components of the electric displacement, $\mathbf{D}$, and magnetic flux, $\mathbf{B}$, fields. The type of boundary conditions used throughout this work are:

- Perfect magnetic conductor (PMC): this condition is used when a boundary reflecting any incident wave is desired. The boundary is an interface

between the simulation domain and a PMC. Because of an infinite conductivity in the PMC the magnetic field here has to be zero. In turn, due to Eq.(2.12), also the tangential components of the field on the boundary has to be null, i.e. $\hat{n} \times \mathbf{H} = 0$.

- Perfect electric conductor (PEC): this condition is the analog of PMC but for the electric field and it is expressed as $\hat{n} \times \mathbf{E} = 0$.

- Periodic boundary condition: the tangential components of the field impinging on such boundaries is periodic. When this condition is employed, it has to be applied on a group of parallel boundaries.

- Continuity boundary condition: it used for internal boundaries and it is expressed by Eqs.(2.11) to (2.14) with $\rho_s = 0$ and $J_s = 0$.

- Perfectly matched layer (PML): this is not strictly speaking a boundary condition but rather an artificial absorbing layer at the simulation domain frontiers. A PML is used to model an open boundary as it completely absorbs any incident wave with very low, ideally zero, reflection.

- Scattering boundary condition: this is a boundary transparent to scattered and incoming plane waves. This boundary condition may be sometimes employed in *COMSOL* instead of building a PML to simplify the simulation domain.

There are many available methods to introduce a source in the simulation domain. The first and easiest to think of is to define the field at a certain point in the simulation domain and plug it directly into Maxwell's equations. However, due to continuity of the tangential field components, this source point would also act as a PMC, if the magnetic field was specified. Another more clever solution is to introduce a soft or current source. In this method instead of directly defining the field, a current source is set. Then due to Ampere's law this will also generate a magnetic field. Because the field at this point is not explicitly specified, no spurious reflections occur at the source points.

In order to illustrate some of the features of FEM simulations explained above, an example of a simulation modeling the interface between two materials of different refractive indices is reported in Fig. 2.3. The refractive index of the two media is 1 and 3. The mesh element distance is $\lambda/10$, where $\lambda = \lambda_0/n$ with n

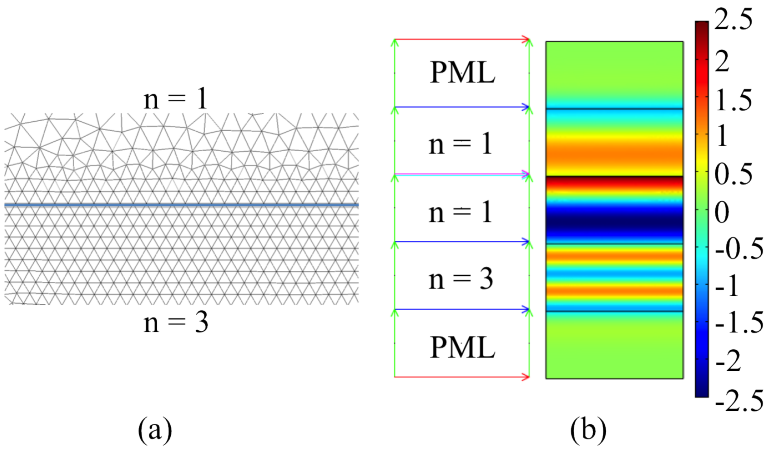

Figure 2.3: (a) Example of a mesh generated for a domain region with different materials. The mesh is more dense where the relative permittivity is higher because the wavelength is shorter. (b) On the left the boundary conditions employed are depicted. The lateral boundaries (green) are periodic boundaries, top and bottom boundaries (red) are set to PMC. On the internal blue boundaries, continuity conditions are used. The top and bottom domains are PMLs. The fuchsia-light blue boundary is the light source and it is transparent to any incident wave traveling upwards, meaning that any incident wave coming from the bottom domains is not reflected by the boundary. The light propagates toward the light blue side. In the surface plot on the right, the electric field is plotted. As the field propagates in different materials, the wavelength changes and reflection occurs.

refractive index of the domain. As seen in Fig. 2.3(a), the mesh is finer in the domains with higher refractive index, because, as also showed in Fig. 2.3(b), the wavelength is shorter. The light source is a plane wave with a wavelength of 1.55 µm traveling towards the lowest boundary. In this model no variations of the domain nor of the fields is assumed in the horizontal direction and therefore periodic conditions are used to model open lateral boundaries. PMLs are employed at the top and bottom of the domain to obtain open boundary conditions. These minimize the artificial reflections from boundaries into the simulation domain. Finally the top and bottom boundaries are set to PMC, as no field is incident on them due to the PMLs. All the boundary conditions used in the FEM simulation are depicted in Fig. 2.3(b).

As previously mentioned, an important simulation parameter is the mesh element size. A too coarse mesh produces non-physical results due to generation of

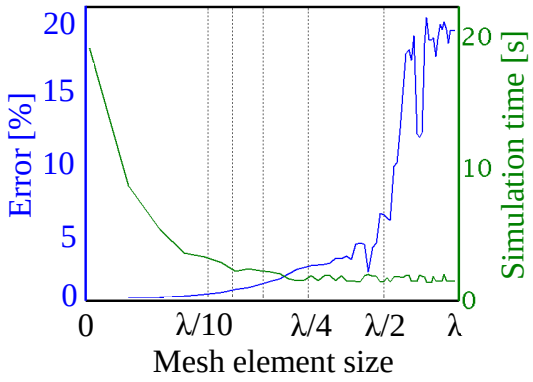

Figure 2.4: Simulation time and relative error between the calculated and theoretical value of the reflection coefficient given by an interface between two dielectrics as a function of the mesh element size. By decreasing the mesh element size, the simulation time increases but the error diminishes and the calculated reflectivity converges to the theoretical value.

numerical artifact, while a too fine mesh uses too many computational resources because the number of mesh elements increases. The reflectivity given by the interface of Fig. 2.3 is calculated using different mesh sizes. The results are plotted in Fig. 2.4. It is important to note that the results converge for mesh element size smaller than $\lambda/10$. In the meanwhile, the simulation time increases exponentially as the mesh element size is reduced. Therefore, to optimize the computational load per numerical simulation and to obtain results with good accuracy, a mesh element distance of $\lambda/10$ is chosen to perform the FEM simulations of this work. Adopting this mesh resolution the value obtained for the reflectivity is 24.9% that is in good agreement with the value given by the Fresnel equations, i.e. 25%.

Chapter 3

Phase Front Engineering

Phase front control can be achieved by careful design of HCG structures. These gratings can be integrated in VCSEL structures to replace Bragg gratings. As previously discussed, this is beneficial for different aspects. In particular, by controlling the phase front directly with the HCG allows to spare additional packaging steps and in turn to reduce the production cost of optoelectronic modules.

This chapter illustrates how it is possible to control the phase response of an HCG in order to tailor the transmission properties. A preliminary design step is used to investigate the transmission spectrum of periodic grating structures, i.e. HCGs with constant periodicity and DC, by using RCWA numerical simulations. From these data, the structural parameters to design non-periodic gratings with wave-front manipulation abilities, that are suitable for VCSEL integration, are found. Finally these structures are investigated using FEM to analyze the phase manipulation abilities.

3.1 Phase control with high-index contrast gratings

Manipulation of the wave-front is often needed in optoelectronic modules. Currently, this functionality is achieved by introducing additional optical components, as lenses, during the packaging process with a consequent negative impact on the costs. An important example is the need to obtain a focused beam out of a light source to maximize the output coupling. In fact the usual output beam of a laser is divergent and it is only successively focused with lenses. These devices

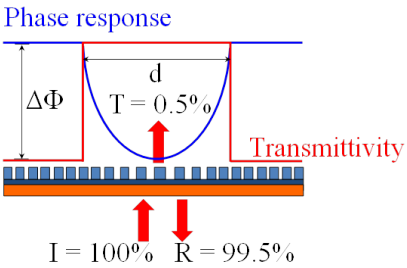

Figure 3.1: The local phase response of the grating depends on the local structural properties as, for example, DC or grating periodicity. By varying these parameters the phase profile of the transmitted beam is modified and it can assume a spatial dependency, while maintaining a high reflectivity.

provide focusing due to a transmission response with a parabolic phase profile: $\phi(x, y) = k_0(x^2/2f_x + y^2/2f_y)$, where x and y are spatial coordinates on the plane orthogonal to the beam propagation direction. A light beam with this phase would focus at a distance f_x, f_y from the phase plane, in the x-axis and y-axis direction respectively. Another interesting feature to obtain could be a linear phase profile: $\phi(x, y) = \alpha_x x + \alpha_y y$. This results in a beam steered to a specific angle that depends on the coefficients α_x and α_y.

The phase response of a periodic HCG at a certain wavelength is spatially independent. The structural parameters that determine the HCG spectral response are grating thickness, t_g, grating periodicity, Λ, duty cycle, DC, low-refractive index material thickness, t_l and the refractive indices of the material used. For wave-front engineering purposes, it is useful to observe that these parameters also determine the phase shift of the transmitted light. If the grating structure is locally changed, the properties of the transmitted beam, such as phase or intensity, will gradually adapt to these variations as depicted in Fig. 3.1. Following this principle it is possible to contemplate non-periodic HCG structures that allow to obtain spatially varying phase profiles, $\phi(x, y)$, in transmission while maintaining a low transmittivity. To facilitate the characterization of these structures, the non-periodic grating with engineered phase profile is located between two different periodic HCG regions with very low transmittivity. With this configuration light is transmitted only through the non-periodic HCG. As illustrated in Fig. 3.1, the total phase shift achieved by the engineered structure of width d is denoted as $\Delta\Phi$.

To successfully integrate this technology in VCSEL systems, two requirements are set on the final grating design. First, in order to employ this technology for high reflectivity mirrors, the transmission has to be low enough to allow lasing and high enough to ensure a useful output power. In this work the useful range of transmission coefficients considered is between 0.4% and 0.6% [2]. Second, to successfully modify the phase of the transmitted light, the structure has to be at least as large as the beam width. Typical values for VCSELs are between 5 µm and 7 µm [2].

3.2 Periodic high-index contrast gratings

By analyzing different periodic HCG structures, the useful key grating parameters needed to realize a HCG with a spatially dependent phase response are found. The transmission spectrum of different HCG is numerically computed using the RODIS implementation of the RCWA method. In order to achieve high reflectivity at the 1550 nm wavelength, the thickness of the HCG investigated is around 500 nm. To obtain a larger range of useful design parameters satisfying the VCSEL integration requirements, the thickness of the SiO_2 layer, t_l, is considered. This parameter affects the interference between the light reflected from the HCG and from the InP-SiO_2 interface. The reflectivity of the entire structure can be enhanced or reduced to meet the transmittivity requirement and thus the range of allowed transmittivity values can be enlarged. It is to note that thicknesses t_l smaller than few nanometers are not considered as it would result in a structure which cannot be fabricated with sufficient accuracy. The phase shift due to reflection from the InP-SiO_2 interface is 0 radians. On the other hand the phase shift, at the same plane, of light reflected from the HCG is given by

$$2k_0 n_l t_l + \phi \tag{3.1}$$

where k_0 is the free-space wave number, n_l is the refractive index of SiO_2, t_l is the SiO_2 layer thickness and ϕ is the phase shift due to reflection from the HCG. Destructive interference can be obtained if the phase difference between the two reflected waves is an odd integer multiple of π:

$$2k_0 n_l t_l + \phi = (2m+1)\pi \qquad m = 0, \pm 1, \pm 2, ... \tag{3.2}$$

Achieving destructive interference in reflection means that transmission is enhanced because of power conservation. Likewise, if the phase difference between the two reflected waves is an even multiple of π, constructive interference would be observed and the transmittivity would be reduced. To calculate the minimum reflectivity required on the HCG in order to have a total minimum reflectivity of 99.4% at the InP-SiO_2 interface of the mirror, the transmission matrix method is applied. The SiO_2 layer is treated as a dielectric block of length t_l located between the InP substrate and the HCG. The total reflection coefficient at the InP-SiO_2 interface provided by the mirror structure is given by

$$r = -r_1 + \frac{t_1^2 r_2 \exp(-2j\beta t_l)}{1 - r_1 r_2 \exp(-2j\beta t_l)} \tag{3.3}$$

where r_1 (t_1) is the reflection (transmission) coefficient from SiO_2 to InP, β is the propagation constant in SiO_2 and r_2 is the HCG reflection coefficient. Assuming a constructive interference of the reflected field, the minimum reflectivity required on the HCG to comply with VCSEL integration requirements is 98.7%.

As far as the fabrication of the final grating is concerned, varying the grating thickness, t_g, to modify the phase front is not feasible due to the multiple etching steps it would imply. Thus, only modifications of the grating periodicity or the DC are considered.

As illustrated in Fig. 3.2(a), a set of useful structural parameters to design HCGs with phase front manipulation abilities for TM polarized incident light at the 1550 nm wavelength is found by varying the DC and the grating period, Λ, while the grating thickness t_g is kept constant at 480 nm. The area delimited by the white line depicts the set of structural grating parameters with a transmittivity between 0.4% and 1.3%. In Fig. 3.2(b) a set of useful parameters for the HCG design is shown. The DC is kept constant at 55%, while Λ is varied. From Fig. 3.2(b) it is observed that the transmittivity initially decreases by increasing Λ, then increases and finally decreases. This behavior is caused by the change of the resonant wavelength of the structure while changing the grating period Λ. In fact, the wavelength of minimum transmission (maximum reflection) is influenced by all the grating structural parameters because the PBG modes of the photonic crystal structure are modified. This behavior is observed in the contour plot of Fig. 3.3(a) where the the dependency of the transmission spectrum on the grating periodicity, Λ, is shown. Furthermore, it is noted that there might be one or two wavelengths at resonance. Depending on the structure these resonances can

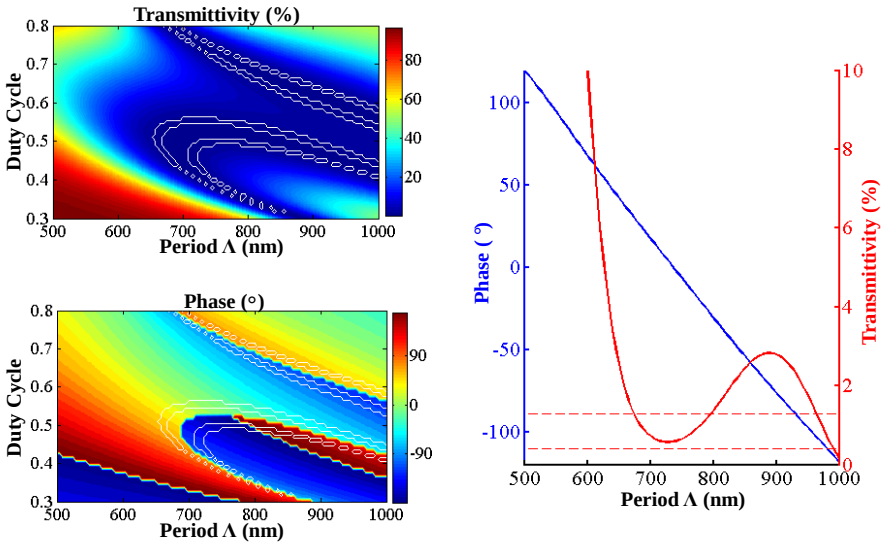

(a) (b)

Figure 3.2: In (a) the transmittivity and phase shift of transmitted light as a function of DC and grating periodicity Λ are shown. The wavelength of the light is 1.55 µm. The white line encloses the area where the transmittivity is between 0.4% and 1.3%. In (b) transmittivity and phase shift values extracted from the contour plots in (a) at a constant DC of 55% are shown. The red dashed lines indicate the range of transmittivity values fulfilling VCSEL integration requirements.

get closer and even merge in only one broader resonance. In the HCGs analyzed, with the DC chosen, the two resonances are merged close to λ =1550 nm. As seen in Fig. 3.3(a), this phenomenon allows to obtain a larger variation of the grating periodicity while maintaining a low transmittivity and thus a larger phase shift is achievable as seen in Fig. 3.3(b).

The characterizations of non-periodic HCGs with wave-front manipulation abilities are performed on a grating implemented on a silicon-on-insulator (SOI) wafer. The grating layer thickness, t_g, of the wafer is 500 nm and therefore a different HCG has to be designed. To facilitate the device characterization, the transmittivity value targeted for the non-periodic grating is 14% ± 1.75%, while the periodic gratings have a transmittivity lower than 0.1%. To accomplish this the grating DC chosen is 53 %. RCWA simulation results showing the transmittivity and phase shift in transmission as a function of the grating periodicity, Λ, are reported in Fig. 3.4.

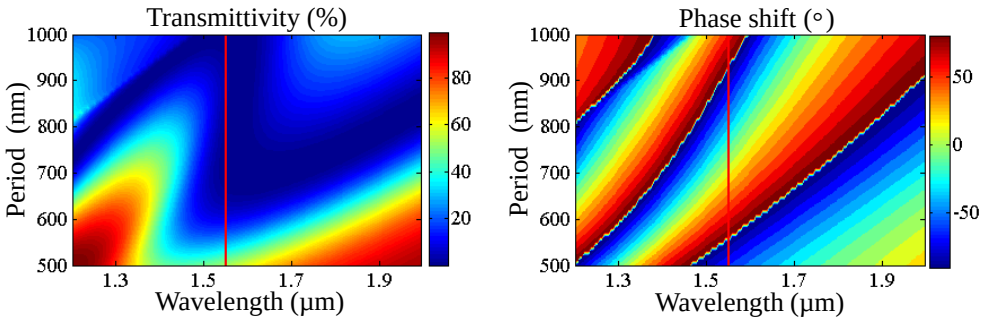

(a) (b)

Figure 3.3: The dependency of the HCG transmission spectrum on the grating period Λ is shown. The DC is 55% and the grating thickness t_g is 480 nm. The values of transmittivity, in (a), and of phase shift, in (b), along the red line are plotted in Fig. 3.2(b).

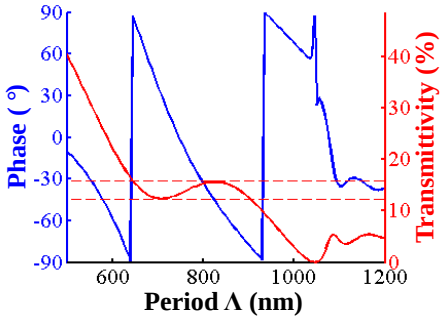

Figure 3.4: Phase shift of transmitted light and transmittivity as a function of the grating periodicity Λ at a wavelength of 1550 nm. The grating parameters are: DC 53%, $t_g = 500\,\text{nm}$ and $t_l = 2\,\mu\text{m}$.

3.3 Non-periodic high-index contrast gratings

As previously mentioned, the grating structural parameters are locally varied in order to master the phase response. This process creates a final structure that is no longer periodic. Therefore, to investigate this scenario RCWA is no longer useful because it requires a periodic grating structure. The method used, instead, is FEM. These numerical simulations are performed using the *RF Module* of *COMSOL*.

Two-dimensional simulations are performed to investigate the designed structures that are one-dimensional gratings. In Fig. 3.5 the simulation domain is depicted. The designed non-periodic grating structure (darker color in Fig. 3.5)

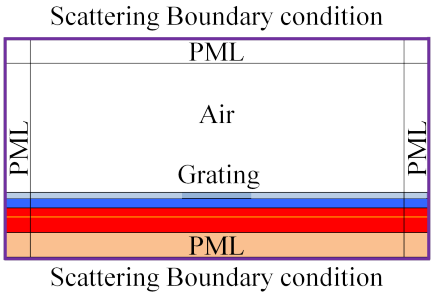

Figure 3.5: Sketch of the simulation domain to numerically investigate the final structures. The boundary conditions have to represent open boundaries and avoid numerical reflections back to the simulation domain. The source is depicted with a yellow line and is set to a TM polarized plane wave at the 1550 nm wavelength with Gaussian power envelope.

is located in the middle of the grating region. The structure is extended to the domain lateral boundaries using a periodic HCG with very low transmittivity, e.g. lower than 0.05%. With this configuration light will be transmitted only through the non-periodic HCG region. PMLs are employed at the sides of the simulation domains. However, in order to avoid artificial reflections from these boundaries, the incident field here has to be very weak. In fact, in *COMSOL*, it has been observed that when interfaces between different materials are present within the PML region, high artificial reflections appear in the simulation domain. This effect, indeed, sets a restriction on the minimum domain width that has to guarantee that at the lateral boundaries the field intensity is very weak or zero.

3.3.1 Beam focusing

Using the design parameters of Fig. 3.4, the grating periodicity is locally varied to achieve a parabolic phase response in transmission: $\phi(x) = k_0(x^2/2f_x)$, where $k_0 = 2\pi/\lambda$ and f_x is the equivalent focal length. In Fig. 3.6 a FEM simulation of the non-periodic HCG designed to have focusing abilities is shown. The light source is TM polarized and it has a wavelength of 1550 nm. The focal length of the structure measured from the intensity profile of Fig. 3.6(a) is $f_x \sim 37\,\mu\text{m}$. As illustrated in Fig. 3.6(c), at $z = f_x$ the beam waist is reduced with respect to the initial beam and the Gaussian power envelope is fairly maintained.

From the RCWA simulation results, assuming that the local phase response

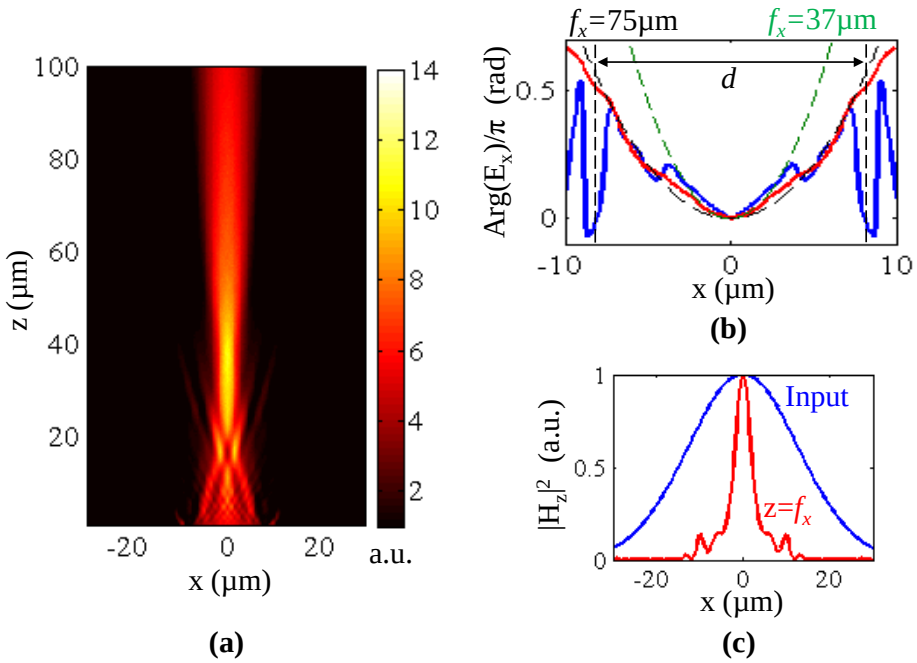

Figure 3.6: Numerical simulation with COMSOL of a grating with parabolic phase response in transmission. (a) Normalized intensity. The focal point is about 37 µm far from the grating. (b) Phase of the electric field as function of x-coordinate at 1 µm from the grating. The transmission phase response obtained from the analyzed sample design is denoted by the blue line. The red line shows the phase profile, at the same z position, of an HCG where the periodic grating has the same periodicity and DC of the extreme ends of the non-periodic HCG region. With dashed lines are drawn parabolic phase profiles with $f_x = 37$ µm and 75 µm. In (c) the input beam (denoted in blue) and beam at the focal point (denoted in red) are compared. The focused beam is almost Gaussian, but the spot size is reduced due to focusing.

depends on the local structural parameters, the total phase shift provided by the designed structure should be $\Delta\Phi = 115°$. The structure width, d, is equal to 17.4 µm. Assuming that the phase profile of the transmitted field is parabolic, the equivalent focal length f_x is given by

$$f_x = k_0 \frac{d^2}{8\ \Delta\Phi} \tag{3.4}$$

and for the current grating design it is estimated to be 75 µm. The difference between the equivalent focal length obtained with FEM simulations and the one calculated based on RCWA simulations is due to the abrupt change of the transmittivity from the non-periodic to the periodic HCG regions. In fact, if the periodic grating had the same periodicity and DC of the extreme ends of the

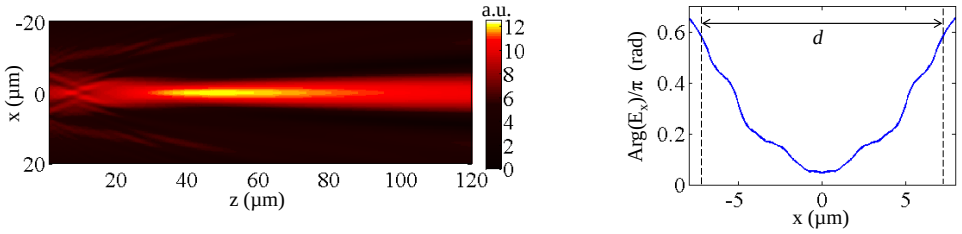

(a) **(b)**

Figure 3.7: Numerical simulation with COMSOL of a grating with parabolic phase response in transmission. (a) Normalized intensity. The focal point is about 50 µm from the grating. (b) Phase of electric field as function of x at 1 µm from the grating is parabolic. The curvature of the phase profile is higher than the curvature of the red profile of Fig. 3.6(b) and thus the focal length is reduced.

non-periodic HCG region, the focal length obtained from FEM simulations would be in good agreement with the one obtained based on RCWA simulations. This is observed in Fig. 3.6(b) where the electric field phase of the analyzed structure (blue line) is compared to the same measurement for the identical non-periodic HCG but with periodic HCG having the same structural parameters of the borders of the non-periodic HCG (red line). The latter shows a very good agreement with a parabolic phase profile with $f_x = 75\,\mu\text{m}$ and, in turn, with RCWA-based values of focal length and total phase shift, $\Delta\Phi$, achieved by the structure.

The relation between the design parameters $\Delta\Phi$, d, the wavelength λ and the equivalent focal length, f_x, of the non-periodic HCG established in Eq. (3.4) will be useful to design HCGs that have to fulfill a certain set of requirements. It is noted that the focal length is directly proportional to the squared of the non-periodic HCG width, d, while it is inversely proportional to the total phase shift, $\Delta\Phi$. Depending on the application, the HCG design will be limited by the need to comply with specific requirements. For instance, if this HCG is employed as an output mirror of a VCSEL, the reflectivity is required to be about 99.5 % for lasing, and the non-periodic HCG size needs to match the mode size that is typically 5-7 μm as specified in Section 3.1. The need to simultaneously fulfill these requirements limits the degree of freedom in controlling the phase response of the grating by reducing the set of available key grating parameters for the final HCG design.

The focal length depends on the curvature of the parabolic phase profile given

by the non-periodic HCG. From Eq. (3.4), at a fixed wavelength, this is determined by the $d^2/\Delta\Phi$ ratio. Varying this parameter the focus can be moved closer or further from the grating. In Fig. 3.7 another example of HCG with focusing abilities is shown. The focal length measured from the intensity profile reported in Fig. 3.7(a) is 50 µm. This is achieved by increasing the curvature of the phase profile (Fig. 3.7(b)) thanks to a reduction of the structure width, d, from 17.4 µm to 14 µm while maintaining the same phase shift $\Delta\Phi$.

3.3.2 Beam steering

Beam steering is obtained with a linearly varying phase response as the one featured by a tilted mirror. A FEM simulation of the grating designed to have beam steering abilities is reported in Fig. 3.8. The light source employed is a plane wave with a Gaussian power envelope with a full width at half maximum of 30 μm and a wavelength of 1.55 μm. The non-periodic grating width, d, equals 6.2 µm. Assuming a plane wave is recovered just after the HCG, the electric field of the transmitted beam can be written as $E(x,z) = E_0(x,z)\exp(-jk_0(x\sin\theta + z\cos\theta))$, where $E_0(x,z)$ is a power envelope, i.e. Gaussian, θ is the angle subtended between the wave vector and the z-axis and $k_0 = 2\pi/\lambda$ is the wavenumber at the wavelength λ. The phase of the electric field is thus given by the argument of the exponential function. In the measure of Fig. 3.8(b) the z-axis coordinate is fixed, thus the electric field phase is a function of only one spatial coordinate: $\phi(x) = -k_0\sin\theta x + \kappa$, where κ is a constant. Comparing this expression to the linearly varying phase of the type $\phi(x) = \alpha_x x$ leads to $\alpha_x = -k_0\sin\theta$. Furthermore, the proportionality factor α_x depends on the phase difference $\Delta\Phi$ achieved by the structure of width d. Due to the linear relation between phase shift and x, the proportionality coefficient is given by $\alpha_x = \Delta\Phi/d$ and, in turn, the steering angle θ is given by

$$\theta = \sin^{-1}\left(\frac{\Delta\Phi}{d\ k_0}\right). \tag{3.5}$$

This equation relates the design parameters $\Delta\Phi$, d and the wavelength λ to the steering angle θ achieved by the structure. It is noted that, at a certain wavelength, higher steering angles can be obtained by increasing the total phase shift, $\Delta\Phi$, throughout the structure or by decreasing the grating width, d. It is also seen that for longer wavelengths, i.e. smaller wave number, the beam

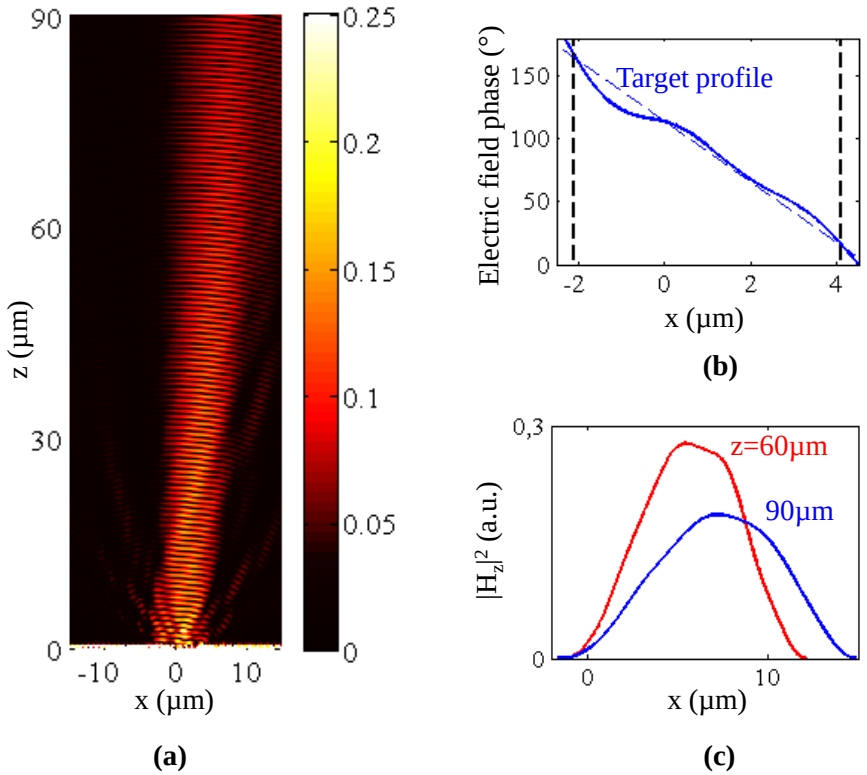

Figure 3.8: (a) Magnetic field intensity profile ($|H_z|^2$). The HCG top surface locates at $z = 0$. (b) Phase profile of the electric field (E_x) at z =10 µm. The black dashed lines delimit the projection of the non-periodic HCG region assuming beam steering to 5.5° and negligible beam divergence. (c) $|H_z|^2$ profiles at z =60 µm and 90 µm.

deflection may increase for a constant $\Delta\Phi/d$ ratio. From the RCWA results of Fig. 3.4, the estimated total phase shift of the non-periodic HCG is $\Delta\Phi = 0.83\pi$ rad. Thus, from Eq. (3.5) the expected steering angle of the structure is 5.98°. From Fig. 3.8(a) and 3.8(c), the measured deflection angle, θ, is 5.5°, which is in good agreement with the value predicted by Eq. (3.5). In Fig. 3.8(b), the phase of the electric field, $\phi(x)$, measured at $z = 10$ μm matches well the desired phase profile. The slight deviation from the targeted linear phase profile can be attributed to the interference with the diffracted near field: The transition from the near- to the far-field occurs around $z \sim d^2/\lambda = 25$ μm [19]. The total phase shift, $\Delta\Phi$ measured in Fig. 3.8(b) is approximately 150° as estimated from Fig. 3.4. These good agreements in θ and $\Delta\Phi$ found between the RCWA-based periodic simulations and the FEM-based non-periodic simulations validate our assumption that local transmission phase is determined by local grating parameters.

A suggested grating design complying with VCSEL integration requirements

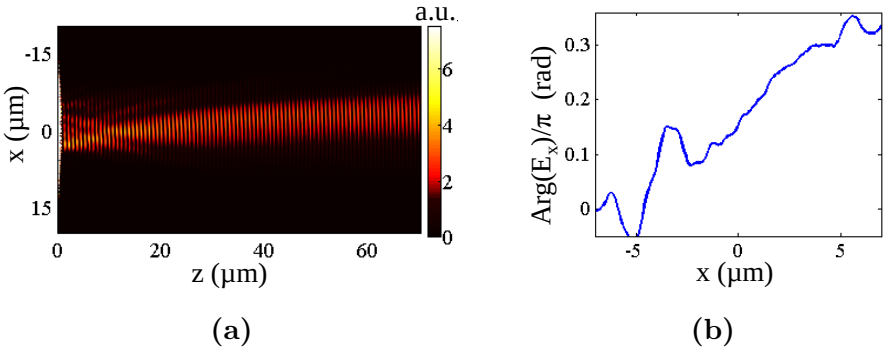

(a) **(b)**

Figure 3.9: Numerical simulation with COMSOL of a grating with linear phase response in transmission. (a) Normalized magnetic field intensity profile ($|H_z|^2$). (b) Phase of electric field as function of x at 1 µm from the grating. From the angular coefficient of the profile, the calculated steering angle from the normal to the grating is approximatively 2°.

is obtained from the RCWA results of Fig. 3.2. This structure is investigated with FEM simulations and the results are shown in Fig. 3.9. From the intensity profile reported in Fig. 3.9(a) the steering angle observed is approximately 2°. In Fig. 3.9(b) the phase profile of the electric field 1 µm from the HCG is shown. Deviations from the targeted linearly varying phase profile may be attributed to near-field interference. From the RCWA-based results of Fig. 3.2, the expected total phase shift is $\Delta\Phi = 0.32\pi$ rad. The width of the designed structure is $d = 7.5$ μm. Thus the steering angle expected from the structure calculated using Eq. (3.5) was 2°, in good agreement with FEM simulation results. From Fig. 3.9(b) it is observed that the total phase shift of the transmitted beam is approximately 0.3π, in good agreement with the RCWA-based result.

As previously observed, the freedom in the engineering of the HCG phase response is limited by the need to comply with additional requirements that depend on the specific application. In particular, the maximum achievable steering angle is limited by this. For instance, to obtain a bigger tilting angle that the one achieved with the HCG simulated in Fig. 3.9(a), the only possibility would be to feature a larger phase difference $\Delta\Phi$ because the structure size d is set by the requirements. However, because the structure reflectivity is limited around 99.5%, the set of structural design parameters found is not large enough and thus a different set should be found.

Chapter 4

Fabrication Process

The fabrication process of the structures designed in the previous chapter is presented. The procedure is very similar to the one performed to fabricate normal periodic HCGs. An electron beam (e-beam) lithography is performed to build a mask of hardened resist on the wafer surface. This layer will protect the top of the grating grooves during the etching step needed to form the HCG. The lithography mask has to reflect the DC or grating periodicity modulation of the non-periodic grating design. Due to the need of steep and narrow profiles, to create the grating grooves a dry etching is performed. This process is preferred because a high anisotropy and selectivity can be obtained.

In order to achieve a real cost-effective solution for VCSEL integration the fabrication process has to be as simple as possible. In this perspective, it would not have been a good solution to modify the grating thickness, t_g, in the design, because of the multiple etching steps it would imply.

4.1 Electron beam Lithography

An e-beam lithography is performed prior to etching in order to create the mask that defines the etched geometry. This lithography technique is essential to obtain features with nanometer precision. The advantage of this technology as compared to UV-lithography is that the pattern transfer is not limited by diffraction. In e-beam lithography a flux of electrons is controlled and directed by a magnetic lenses system. If a positive resist is employed, the area exposed to the beam of electrons becomes soluble in a solvent. In Fig. 4.1(a) a sketch of the sample after

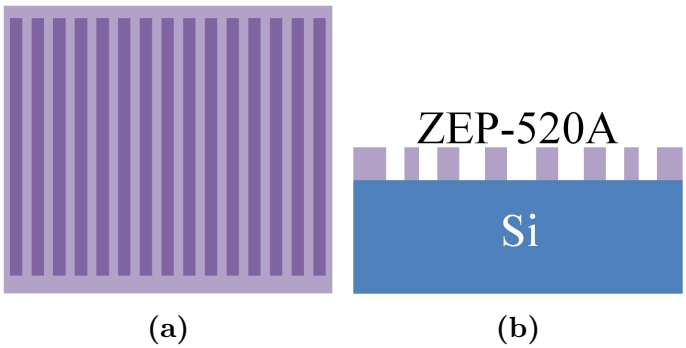

Figure 4.1: Sketch of the wafer surface after exposure, (a), and developing, (b). In the top view of (a) the exposed resist is indicated with a darker color. In (b) a side view of the sample through the grating structure after developing. The only resist left is on the grooves top.

exposure is shown. The exposed areas are represented in a darker color and these are the regions where the resist will be removed with the developing process.

In the fabrication process performed, a 200 nm layer of ZEP-520A is spun on the surface of an SOI wafer. The ZEP-520A is a very high resolution positive tone resist employed for e-beam lithography. The spun thickness has to ensure that, during the etching, the resist is not completely removed. If the resist was completely etched away during etching, the grooves would result thinner and with smoother edges than designed, modifying the DC of the grating. To chose a safe resist thickness, the selectivity of the etching has to be considered. In the etching employed the selectivity of ZEP-520A versus Si is approximately 1:7, thus a layer of 200 nm of ZEP-520A is sufficient to etch 500 nm of Si, being the grating thickness, t_g, 500 nm.

After spinning, the samples are pre-baked for 2 minutes at 180°C to dry off excess of solvent. The developing is performed dipping the wafer for 2 minutes in ZED-N50. To stop the chemical reaction dissolving the resist, the samples are placed for one minute in Isopropanol. Finally, the wafer is further cleaned by squirting Isopropanol on the developed surface and a blow drying with a nitrogen flow is performed.

In Fig. 4.1(b) the final result after developing is depicted. The resist is removed from the surfaces that have to be etched to form the grating grooves.

4.2 Dry Etching

After developing, the samples are dry etched with a deep reactive ion etching (DRIE). This etching technique is highly anisotropic and it is used to create deep, steep-sided features. A Bosh process is employed for the dry etching. The etching is cyclic, each cycle having two parts. In the first part the sample surfaces are passivated by depositing a chemically inert layer. This layer has a composition similar to Teflon and it is obtained introducing a C_4F_8 gas flow in the chamber. In the second part of the cycle, the etching takes place using a plasma of C_4F_8 and SF_6. During this time slot the passivation layer is removed by ion bombardment, leaving reactive surfaces that are chemically etched. The duration of the two time slots and the gas flows, among other parameters, influence the etching properties. To obtain a controlled process, the passivation layer has to be thick enough to protect the sidewalls throughout the etching time but not too thick that actually prevents etching of the flat surfaces. Therefore a trade-off between passivation and etching has to be found.

In this project it has been tried to find the optimal etching conditions for a new installed DRIE machine in the Danchip cleanroom. The strategy followed was to start from an existing recipe used on the former machine at Danchip and adapt it to the new machine. To perform the process optimization, gratings with a period of 700 nm and duty cycles varying from 0.1 to 0.9 have been fabricated. Initially, different samples have been etched with different number of cycles to measure the etching rate and observe whether the process was constant during all the cycles. From scanning electron microscope (SEM) images of this first test sample it was noted that the etching rate of Si was about 30 nm/cycle and it was not significantly varying from cycle to cycle. This result is close to the 40 nm/cycle of the old etching machine. However, after 6 etching cycles, the duty cycle of the grating was approximatively 10% lower than designed. Therefore the main problem to solve was to obtain a more selective etching. To pursue this goal, different strategies have been applied. First, an extra time where only the gasses where introduced into the chamber was added before each passivation and etching time slot. This was done in order to ensure constant initial conditions before each cycle. In fact, some oscillations of the reflected RF power and measured gas flows were observed during the first tests and this might have influenced the process dynamics. Indeed an improvement of the etched features

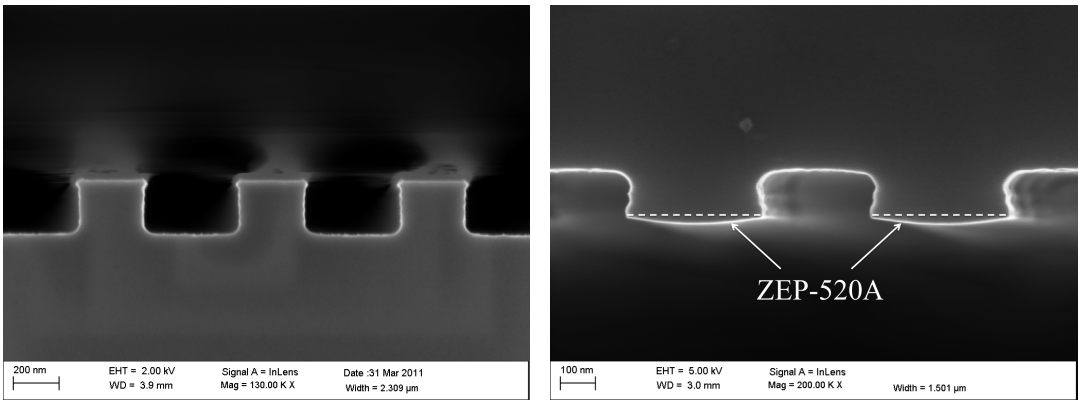

(a) **(b)**

Figure 4.2: SEM images of the test structures used to find the right etching conditions. In (a) the shape of the grooves is acceptable but their width is much thinner than designed due to lateral over etch. In (b) a post-baked samples showing that a very thin layer of resist is left on the grooves top.

was obtained by following this strategy, but again the overetch observed was not controlled and it was decreasing while the duty cycle was increasing. The best results with this technique were obtained by adding an extra time of 3 seconds before each passivation and etching time slot. The second attempt has been to try to use carrier wafers of either Si or SiO_2 to modify the overall etching area. In fact, SiO_2 is etched at a much lower rate than Si in the process performed, and thus, this affects the chemical etching component of the process. By decreasing the etching area, the local concentration of the radicals involved into chemical reaction is increased and, in turn, the chemical etching component of the process is increased. Typically, decreasing the chemical etching component increases the anisotropy of the etching but reduces the selectivity and the etching rate [7]. This test confirmed that the best solution for this recipe was to use a Si carrier instead of a SiO_2 one. The result after 6 etching cycles using an Si carrier wafer and with an extra time of 3 seconds before each cycle is shown in the SEM image of Fig. 4.2(a). The etched depth is approximately 240 nm, with an etching rate of 40 nm/cycle that is equal to the one achieved with the old machine. The groove shape is acceptable with steep edges, but the width is 280 nm instead of 350 nm as designed. This lateral over etch is too significant and it has to be diminished in order for this recipe to be employed in the fabrication process. Finally, in order to improve the selectivity of the etching, post-baking of the wafer for 4 minutes

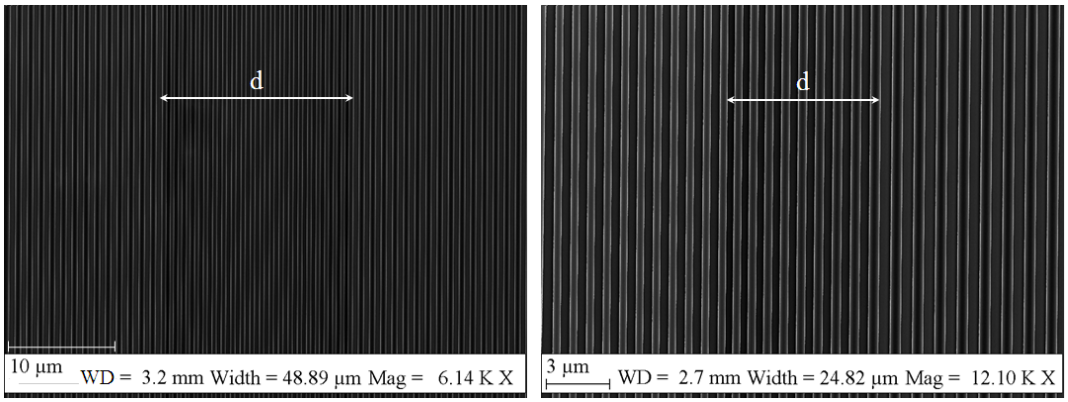

(a) **(b)**

Figure 4.3: SEM images of the structures fabricated for the characterization experiments. In (a) the grating with parabolic phase response is shown. The non-periodic HCG width, d, is recognizable as the period modulation occurs only within this region. The etching depth measured was, as expected, 500 nm. In (b) a SEM image of the non-periodic grating with linear phase response is shown.

at 180° was performed. This slightly improved the selectivity of Si versus ZEP-520A, because post-baking hardens the resist, but the main problem as revealed from the SEM image in Fig. 4.2(b) was that the resist etching rate was too high. After 3 cycles the resist was almost completely removed from the grooves top, and this observation is indeed consistent with the previously observed large lateral over etch.

To find the optimal etching conditions would require a more prolonged and thorough work of processing engineering to explore all the variety of process parameters. In this work, due to a limited amount of time available for this purpose, the optimization of the process has not been completed. Further attempts might experiment different gas flows of C_4F_8 to increase the passivation layer thickness and in turn to increase the selectivity of the etching.

To produce the samples characterized in Chapter 6, the older advanced silicon etcher is used. This machine is able to provide the features needed for the structures fabricated in this project. The etching rate of Si is measured by scratching the sample before and after 6 etching cycles. From profile measurements with dektak, circa 250 nm of resist have been removed, giving a calculated etching rate of approximatively 41 nm/cycle. To completely etch through the top Si layer of 500 nm of the SOI wafer 13 etching cycles are performed on the samples. After

etching the residual resist on the sample is removed with an oxygen plasma. In Fig. 4.3 SEM images of the fabricated samples are shown.

Chapter 5

Characterization

In order to demonstrate of the feasibility of the structures proposed and numerically investigated in the previous chapters, HCGs with an engineered phase response in transmission are fabricated following the procedure outlined in Chapter 4 and then experimentally characterized. The measured values are compared to the theoretical values obtained from numerical simulations in Chapter 3 and a good agreement is found.

5.1 Experimental Setup

In Fig. 5.1 the experimental setup used for the characterization experiences performed to proof HCGs with wave-front manipulation abilities is depicted. The light source is a tunable laser emitting at a wavelength of 1.55 µm. The laser output is coupled to a polarizer that can select a linear or elliptical polarization. For the experiments hereby described, linear polarization is adopted. Finally, the light is collected by a photonic crystal (Phc) fiber with a mode diameter of 10 µm. This type of fiber is employed to maintain the laser beam polarization while the light propagates through the fiber. The structures are illuminated from the backside of the SOI wafer, i.e. the substrate Si layer, which has a thickness of about 650 µm. The output beam from the polarization-maintaining photonic crystal fiber is divergent and thus at the silica-grating interface the mode dimension will be about 100 µm. Therefore, in order to avoid the use of additional lens systems to adapt the spot size of the input laser beam to the non-periodic HCG region size, d, the transmittivity of the sample is modulated as explained in

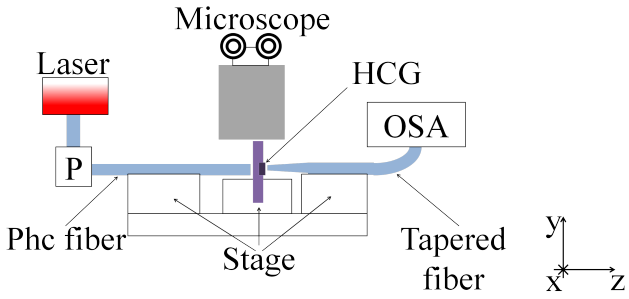

Figure 5.1: The setup used for the characterization experiences is depicted. The laser beam is polarized with a polarizer (P) and then coupled to a polarization-maintaining photonic crystal (Phc) fiber. The light transmitted through the sample is collected with a tapered fiber that is coupled into an optical spectrum analyzer (OSA).

Sec. 3.1. The light transmitted through the sample is collected using a tapered fiber with a mode dimension of 2 µm. The other end of this fiber is coupled into an optical spectrum analyzer (OSA). The waist of the transmitted beam should be around 5-10 µm, i.e. about the width of the non-periodic HCG, therefore the tapered fiber with the smallest spot size available has been used to conduct the measurements.

Both the Phc and tapered fibers are mounted on two stages that can be independently moved in all the three spatial directions (x, y and z) with a precision of ± 0.5 µm. The stage with the sample holder can be moved independently from the two fibers in the x-axis direction.

In order to observe the sample and to perform the setup alignment, two optical microscopes are used. One provides a top view of the setup, while another one allows a lateral view. With the top microscope (depicted in Fig. 5.1) it was possible to measure the distance from the fibers to the sample in the z direction. The lateral microscope was used to observe the position of the fibers in the x-y plane relative to the HCG structure of interest during the alignment procedure.

5.1.1 Alignment

A crucial operation to perform prior to conduct the measurements is the setup alignment. The fibers have to be aligned with respect to each other in order to obtain maximum coupling efficiency and, at the same time, they have to be aligned with the investigated HCG structure. The gratings with phase front engineering

abilities are only about 15−6 µm wide while the overall grating structures have a total width of 400 µm. Thus the lateral optical microscope is necessary for the alignment.

The procedure followed in the setup alignment might be divided into three steps. First, the tapered fiber is aligned in the y-axis direction with the targeted structure using the lateral microscope. Second, the two fibers are aligned with respect to each other without the sample between them. This is performed observing the light power measured by the OSA while moving only the photonic crystal fiber, as the tapered fiber is already aligned to the structures in the vertical direction. Third, using the lateral microscope to observe the tapered fiber, both fibers are aligned with the structure of interest by moving the sample stage in the x-axis direction. This coarse alignment is performed measuring the distance from one end to the other of the overall structure. The distance between the fibers and the sample surface is determined using the top microscope view. Finally, a finer alignment is obtained by slightly moving the sample stage to maximize the coupled power. This is performed using the OSA.

5.2 Beam Focusing

The non-periodic HCG with parabolic phase profile shown in Fig. 3.6 is fabricated following the procedure outlined in Chapter 4. Using the setup described in Section 5.1, the power of the light transmitted through the grating is measured along the x-axis direction and at different distances, z, from the HCG. The results are reported in Fig. 5.2. in Fig. 5.2(a) the measurements are fit to a Gaussian profile to render beam propagation in three-dimensional space. The measurements taken at some different z positions, fitted to a Gaussian profile, are also shown. As illustrated in Fig. 5.2(b), the peak power increases with z to reach a maximum at 50 µm from the grating and decreases afterwards. In the meanwhile, the beam width shrinks and it reaches a minimum at the same z position. These measurements, compared to the ones performed for a periodic HCG, clearly indicate beam focusing at $\sim$ 50 µm from the grating. The equivalent focal length of the structure was expected to be bigger than the one predicted by numerical simulations because the light source used for the characterization was a divergent laser beam. In addition, some uncertainty in determining the absolute distance

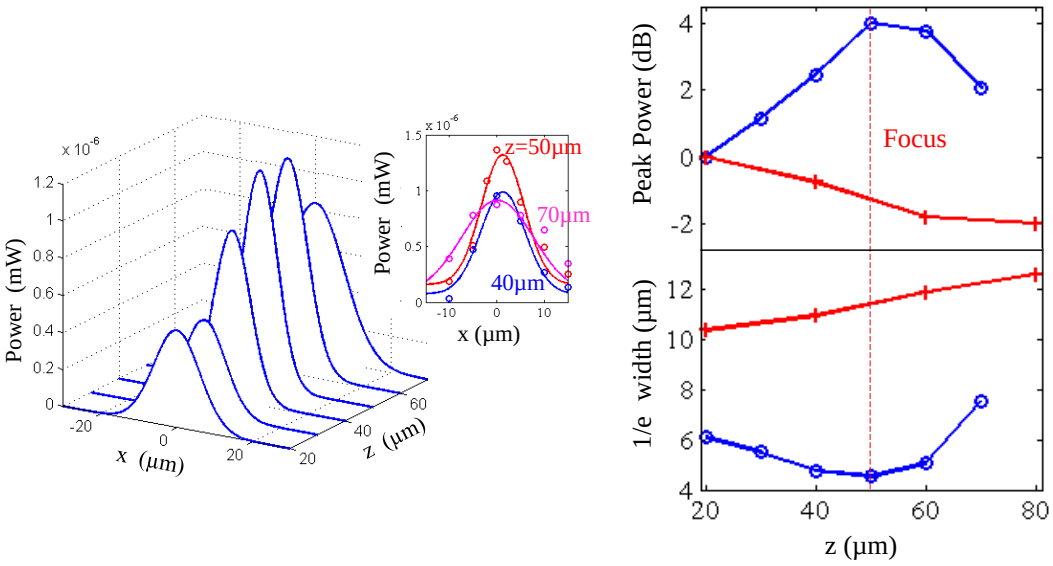

(a) **(b)**

Figure 5.2: In (a) the measurements are fitted to a Gaussian profile to depict the beam propagation. In the right-upper figure part the measurements (hollow dots) and the fits (continuous lines) at different positions are shown. In (b) the measured peak power, normalized to the power at $z = 20\,\mu\text{m}$, and $1/e$ beam width calculated from the Gaussian fits are shown as function of z. Hollow dots denote grating with focusing abilities measurements while pluses denote periodic HCG measurements.

from the HCG plane is introduced by the setup (approximately $\pm 5\,\mu\text{m}$). Therefore these results appear to be in good agreement with the theoretical values for the considered grating design.

5.3 Beam Steering

The non-periodic HCG with linearly varying phase profile simulated in Fig. 3.8 is fabricated following the procedure outlined in Chapter 4. Using the setup described in Section 5.1, the power of the light transmitted through the grating is measured along the x-axis direction and at different distances, z, from the HCG. In order to avoid the complex transient fields from the near- to the far-field, the measurements start from z =30 µm. The measurement results are presented in Fig. 5.3. The spatial position of the peak clearly shifts as the beam propagates further from the grating, indicating beam deflection. As illustrated in Fig. 5.3(a),

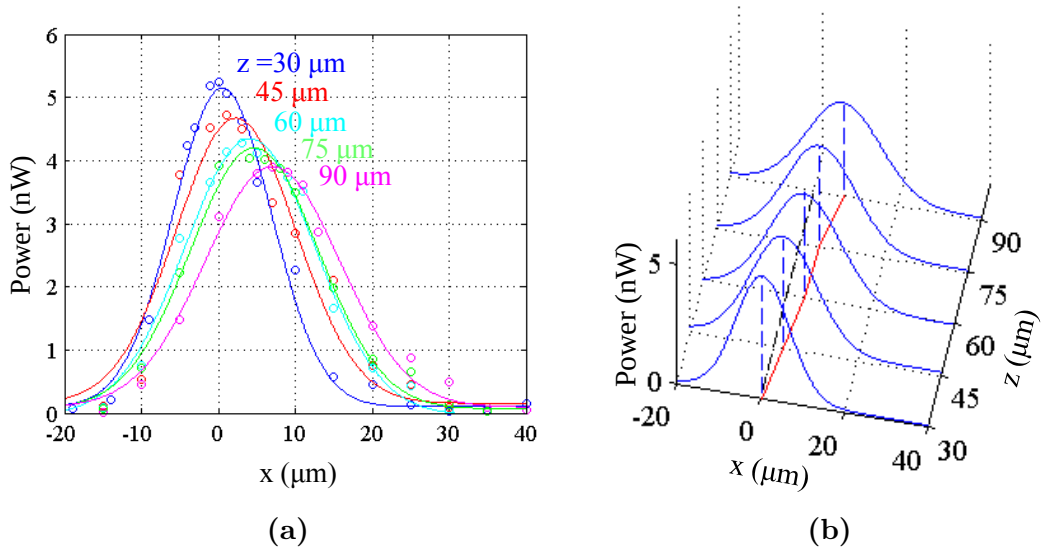

Figure 5.3: In (a) measured (hollow dot) and fitted (line) power profiles at different distances from the HCG are shown. In (b) the Gaussian fits are used to represent the beam propagation. The peaks are projected onto the x-z plane and their movement is revealed by the red line.

the measurements are fitted to a Gaussian distribution. The difference between the fitted curves and the measurements may have several explanations. First of all, due to beam steering, the beam profile would not be exactly Gaussian along the x-axis as the wave front would be tilted by an angle θ with respect to the x-axis. Furthermore, some uncertainty is introduced by the setup. The error in the position of the fibers was $\pm 0.5\,\mu\text{m}$. From the Gaussian fits, the peak is displaced by approximately $7\,\mu\text{m}$ from the first to the last measurements taken at a distance of $30\,\mu\text{m}$ and $90\,\mu\text{m}$ from the HCG, respectively. The measured steering angle is $\theta = \tan^{-1}[7/(90-30)] = 6.65^\circ \pm 0.71^\circ$. This value is in excellent agreement with the theoretical values for the considered grating design, including the prediction by Eq. (3.5). These results are also reported in [20].

Chapter 6

Conclusion

In this thesis high-index-contrast grating (HCG) reflectors that can be used to manipulate the transmitted beam, while simultaneously maintaining high reflectivity for the incident beam have been demonstrated. Fabricated structures non-periodic HCG structures with parabolic phase profile show beam focusing at about 50 µm from the grating. Experimental characterization of non-periodic HCG with linearly varying phase profile show a beam deflection of $\sim 6°$. These findings are in good agreement with numerical simulations. Basic design rules to realize gratings that impose an engineered phase front to the transmitted beam are explained and their applicability is demonstrated by comparison with simulation and characterization results. The ability of these HCGs to feature high reflectivity as well as wave front control can be advantageous for many applications, such as low cost laser fabrication. Furthermore, this approach can be generalized to obtain different phase profiles from the grating, broadening the set of possible applications as well as opening the possibility for integration of additional functionalities in compact and cheap devices.

Appendix A

Articles Written From This Thesis

In this appendix the articles written during the period of this master thesis are presented. An article about gratings with beam steering abilities has been submitted to Optics Express. The concept of phase control by engineering HCG structures is explained and gratings featuring beam steering are suggested. Design rules are derived and their validity is supported by either numerical simulation and experimental characterization results. The full text of the article is reported in the following pages. Another article is being written and it will be submitted to Photonics Technology Letters. This article will suggest HCGs with focusing abilities.

High-index-contrast grating reflector with beam steering ability for the transmitted beam

Luca Carletti, Radu Malureanu, Jesper Mørk, and Il-Sug Chung*

DTU Fotonik, Department of Photonics Engineering, Technical University of Denmark, DK-2800 Kgs. Lyngby, Denmark

*ilch@fotonik.dtu.dk

Abstract: High-index contrast grating mirrors providing wave front control of the transmitted light as well as high reflectivity over a broad bandwidth are suggested and both numerically and experimentally investigated. General design rules to engineer these structures for different applications are derived. Such grating mirrors would have a significant impact on low cost laser fabrication, since a more efficient integration of optoelectronic modules can be achieved by avoiding expensive external lens systems.

©2011 Optical Society of America

OCIS codes: (050.6624) Subwavelength structures (140.7260); Vertical cavity surface emitting lasers.

References and links

1. C. F. R. Mateus et al., "Broad-band mirror (1.12-1.62 μm) using a sub-wavelength grating", IEEE Photon. Tech. Lett. **16**(7), 1676-1678 (2004).
2. M.C.Y. Huang at al., "A surface-emitting laser incorporating a high-index-contrast subwavelength grating", Nat. Photon. **1**, 119-122 (2007).
3. I.-S. Chung, J. Mørk, P. Gilet, and A. Chelnokov, "Subwavelength grating-mirror VCSEL with a thin oxide gap", IEEE Photon. Tech. Lett. **20**(2), 105-107 (2008).
4. I.-S. Chung, et al., "Broadband MEMS-tunable high-index-contrast subwavelength grating long-wavelength VCSEL", IEEE J. Quant. Electron. **46**(9), 1245-1253 (2010).
5. I.-S. Chung and J. Mørk, "Silicon-photonics light source realized by III-V/Si-grating-mirror laser", Appl. Phys. Lett. **97**, 151113 (2010).
6. D. Fattal et al., "Flat dielectric grating reflectors with focusing abilities", Nat. photon. **4**, 466-470 (2010).
7. M. G. Moharam and T. K. Gaylord, "Rigorous coupled-wave analysis of planar-grating diffraction", J. Opt. Soc. Am. A **71**(7), 811-818 (1981).
8. M. G. Moharam et al., "Formulation for stable and efficient implementation of the rigorous coupled-wave analysis of binary gratings", J. Opt. Soc. Am. A **12**(5), 1068-1076 (1995).
9. L. A. Coldren and S. W. Corzine, *Diode lasers and photonic integrated circuits*, p. 438 (Wiley, New York, 1995).

1. Introduction

Recently, high-index-contrast gratings (HCGs) have attracted attention due to their novel characteristics [1-6]. A HCG is a single layer structure with an inscribed one- or two-dimensional sub-wavelength-scale periodic patterning that can provide very high reflectivity over a broad bandwidth [1]. Thanks to a simple and compact structure, HCGs are strong candidates to replace conventional Bragg reflectors, as applied e.g. in vertical-cavity surface-emitting lasers (VCSELs). Also, the ability to strongly modify the grating properties, e.g. via the duty cycle (ratio of a dielectric part width over periodicity), enables the engineering of grating reflectors for a number of different applications. These include simpler epitaxial structure [2], high differential efficiency [2], strong single-transverse-mode operation [3], broad wavelength tunability [4], polarization control [2-5], and light emission into an in-plane silicon photonics chip [5]. Another interesting property of HCGs is that the phase of the reflected or transmitted light can be controlled, while maintaining a high reflectivity. Recent

work [6] has demonstrated that the reflected light can be focused by introducing a parabolic phase front to the reflected beam through the spatial modulation of the grating duty cycle. For integration into VCSELs, phase front control over the transmitted beam is highly interesting, since this would enable to steer the propagation direction of the output light as well as focusing. For example, as illustrated in Fig. 1(a), the light collection from multiple VCSELs to an optical fiber could be facilitated by directly steering the output light from each VCSEL element. This integrated approach would eliminate the need of an external lens for beam collection (Fig. 1(b)). As illustrated in Fig. 1(c), dynamic beam steering would be possible if the refractive index of the HCG could be controlled, e.g. by using the electro-optic effect or the free-carrier plasma effect. These novel functionalities would considerably reduce the lens/optics packaging cost and provide design flexibility in the packaging and free-space optical interconnects. So far, there has been no extensive investigation of the beam steering of the transmitted beam.

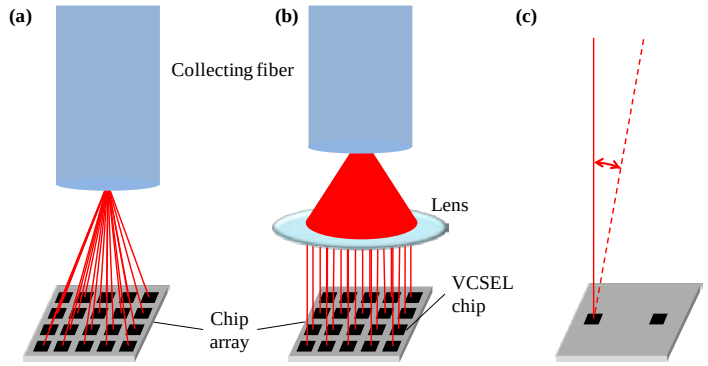

Fig. 1. (a) Light coupling from multiple VCSEL elements to an optical fiber by using HCGs. (b) Light coupling by using a lens. (c) Beam propagation angle can be dynamically steered between the solid and dashed lines by changing the refractive index of the HCG.

In this paper, we investigate the fundamental ability of an HCG to manipulate the phase front of a transmitted light beam and formulate useful design rules for the realization of practical structures. Based on these rules, HCG structures are fabricated and experimentally demonstrated to have beam steering ability. Such structures are promising for replacing the output mirror in VCSELs.

The paper is organized as follows. In Section 2, the simulation methods employed to determine the properties of periodic and non-periodic HCG structures are briefly described. In Section 3, the HCG design issues as well as the characterization set-up are discussed. The procedure to design a HCG structure with a linearly varying phase profile that complies with additional application requirements is explained. In Section 4, numerical simulations and experimental characterization results are presented that demonstrate the beam steering ability of HCGs. The theoretical rules are compared with the measurements and good agreement is found.

2. Simulation methods

In this work two different kinds of HCGs are analyzed. First, the transmission and reflection properties of periodic gratings are investigated using the rigorous coupled-wave analysis (RCWA) method [7, 8]. In this approach the periodicity of the structure is exploited to solve Maxwell's equations. A linear system of equations is built from the boundary conditions. The system solution yields the field distribution, as well as the transmission and reflection characteristics. Extensive simulations are performed to find sets of HCG parameters that provide the targeted transmission phase and transmittivity.

Second, based on RCWA results, grating key parameters are varied within the structure to realize non-periodic HCGs featuring the desired phase profile. It is assumed that the local phase response and the local transmittivity of the non-periodic HCG structure depend on the local grating parameters. This assumption is proven later in Section 4. The commercial software COMSOL implementing the finite element method (FEM) is used to simulate the non-periodic structure. Perfectly matched layers are employed at the simulation domain boundaries.

3. HCG design, fabrication, and characterization set-up

The HCG is a one- or two-dimensional photonic crystal slab surrounded by low refractive index materials. The HCG structure investigated in this paper is depicted in Fig. 2. The grating is implemented in the top Si layer of a silicon-on-insulator (SOI) wafer. For VCSEL integration, the grating layer and the substrate layer in Fig. 2(a) can be III-V semiconductors while the low index material layer can be air [2] or oxide [3]. The structural parameters, i.e., grating thickness, t_g, low-index layer thickness, t_l, grating periodicity, Λ and grating duty cycle, as well as the refractive indices of the materials employed, n_h and n_l, determine the spectral properties of a periodic HCG. Since varying t_g is not feasible due to the multiple etching steps it would imply, here only variations of Λ and the duty cycle are considered. The refractive indices of Si (n_h) and buried SiO_2 (n_l) of the SOI wafer are 3.47 and 1.47, respectively. From the simulation results, the grating thickness t_g is chosen to be 500 nm, allowing a large transmission phase change $\Delta\Phi$ at the target wavelength of 1.55 µm. As shown in Fig. 2(a), a non-periodic HCG of width d is located between two different periodic HCGs. The transmittivity within the non-periodic HCG region is designed to be higher than those of the two periodic HCG regions in order to have the light transmitted only from the non-periodic HCG region.

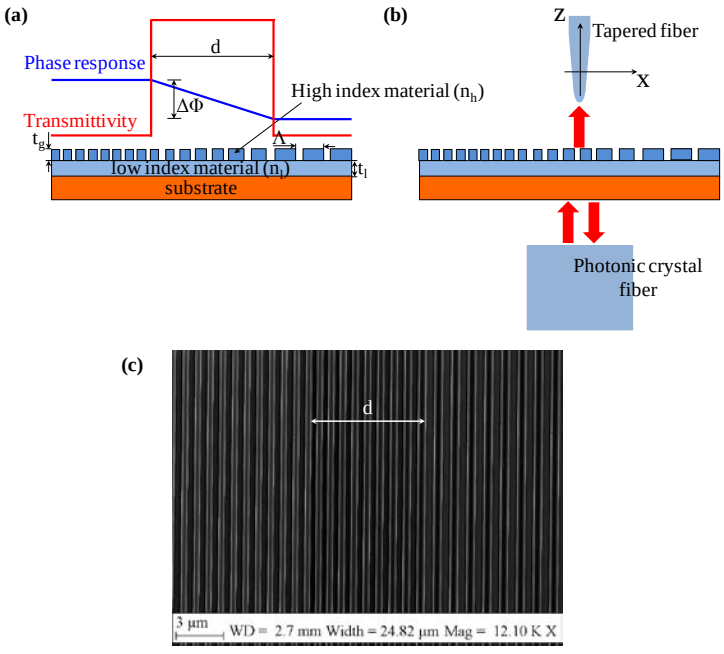

Fig. 2. (a) Schematic of the investigated HCG sample, with the resulting spatially modulated transmission phase response and transmittivity profile. (b) Illustration of characterization set-up. (c) Scanning electron microscope image of the fabricated HCG structure.

Within the non-periodic HCG region, the local phase, $\Phi(x,y)$ of the transmitted light is designed to vary linearly by gradually changing the grating structural parameters. In this implementation, the grating periodicity Λ is varied along the x-axis, while the duty cycle is kept constant. Thus, the phase profile becomes x-dependent, $\Phi(x)$. If necessary, variation along the y-axis also can be introduced. In the left and the right periodic HCG regions, different Λ values and duty cycles are applied.

To deflect a beam to a specific angle, θ, the phase response should be linearly varying in space, $\Phi(x)=\alpha_x x$, where α_x is a proportionality factor and has the unit of rad/m. The steering angle, θ depends on α_x: Assuming a plane wave is recovered just after the HCG, the transmitted electric field may be expressed in the form $E=E_0(x)\exp[-jk(x\sin\theta + z\cos\theta)]$, where $E_0(x)$ is a slowly-varying power envelope and $k=2\pi/\lambda$ is the wave number at the wavelength λ. For a fixed z coordinate, the phase of the field is only a function of x: $\arg(E)=\Phi(x)$. When the phase in this direction is given by a linearly varying profile, the beam would be deflected to an angle of $\theta=\sin^{-1}(\alpha_x/k)$. As shown in Fig. 2(a), the total phase difference between the extremes of the HCG is $\Delta\Phi$, and thus the proportionality coefficient is $\alpha_x=\Delta\Phi/d$. Substituting this in the expression above to estimate the deflection angle gives

$$\theta = \sin^{-1}\left(\frac{\Delta\Phi}{d\cdot k}\right). \qquad (1)$$

This equation relates the design parameters $\Delta\Phi$, d and the wavelength λ to the steering angle θ achieved by the structure. It is noted that at a certain wavelength, larger steering angles can be obtained by increasing the total phase shift, $\Delta\Phi$ throughout the structure or by decreasing the grating width, d. It is also seen that for longer wavelengths, i.e. smaller wave number, the beam deflection may increase for a constant $\Delta\Phi/d$ ratio.

The relationship expressed in Eq. (1) will be useful to design HCGs that have to comply with a set of specific requirements which depend on the application. For example, if the HCG is to be employed as the output mirror of a VCSEL, the reflectivity is required to be about 99.5 % for lasing, and the non-periodic HCG region size needs to match the mode size that is typically 5-7 μm [2]. The need to simultaneously fulfill these requirements limits the degree of freedom in controlling the phase response of the grating.

In Fig. 2(b), the characterization setup is depicted. A polarized laser beam with a wavelength of 1.55 μm is coupled to a photonic crystal fiber. The selected polarization is transverse magnetic (TM) with the electric field vector in the x-axis direction. From the polarization-maintaining photonic crystal fiber with a mode diameter of 10 μm, the beam diverges to a width of about 100 μm at the silica-grating interface. From the transmission side, light is detected using a tapered fiber with small mode dimension (2 μm). In order to avoid the use of additional lens systems to adapt the spot size of the input light to the non-periodic HCG region size, d, the transmittivity of the sample is modulated as shown in Fig. 2(a). The total structure, including both non-periodic and periodic regions, is a square of 400×400 μm^2 that covers all the area illuminated by the incident light.

The fabrication is performed on an SOI wafer. Electron-beam lithography is performed in order to create a mask for the dry etching of grating grooves. To ensure a high selectivity and anisotropy, a Bosh process is employed for the dry etching: The etching is cyclic, each cycle having two parts. In the first part, the sample surfaces are passivated by depositing a chemically inert layer obtained from C_4F_8. In the second part of the cycle, the etching takes place using a plasma of C_4F_8 and SF_6. During this part, the passivating layer is removed by ion bombardment, leaving reactive surfaces that are chemically etched. Figure 2(c) shows an example of a fabricated sample.

4. Results and discussion

Simulation results for the dependence of HCG transmittivity and phase on key grating parameters are shown in Fig. 3. The results were obtained by using the RCWA method. In the HCG design, to facilitate the device characterization, the transmittivity value targeted for the

non-periodic HCG region is 4±0.5%, while in the periodic HCG regions the transmittivity is lower than 0.1%. To accomplish this, the duty cycle in the non-periodic HCG region is chosen to be 53%. With the parameters obtained from Fig. 3(b), the maximum phase shift that can be obtained, while keeping within the range of allowed transmittivity values, is approximately ΔΦ=150°. The non-periodic HCG region is designed to have a width, *d*, of 6.2 μm. The corresponding steering angle of the final device, estimated using Eq. (1), is θ = 5.98°.

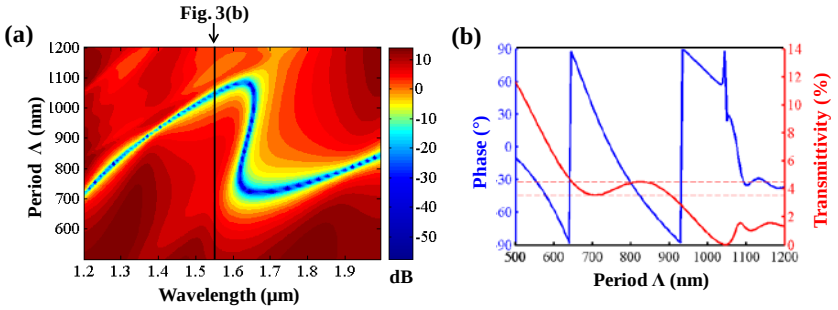

Fig. 3. (a) Contour plot of transmittivity (in dB, color scale) versus wavelength and grating period. The vertical black line corresponds to a wavelength of 1.55 μm. (b) Phase and transmittivity as a function of grating periodicity, Λ, for a wavelength of 1.55 μm.

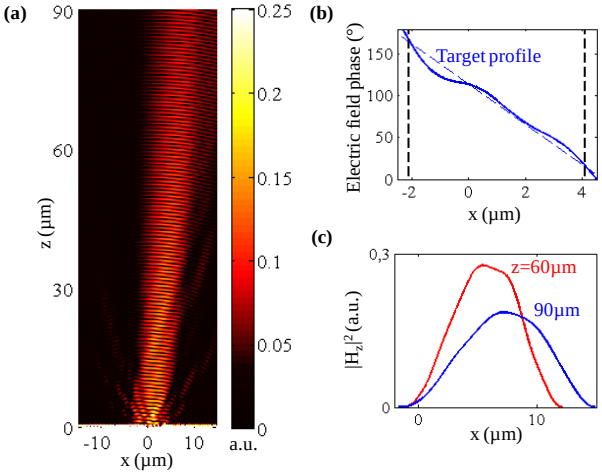

Fig. 4. Simulation results for HCG grating designed for beam steering. (a) Evolution of magnetic field intensity profile ($|H_z|^2$) with distance z from the HCG top surface, located at z=0. (b) Phase profile of the electric field (E_x) at z=10 μm. The black dashed lines delimit the projection of the non-periodic HCG region assuming negligible beam divergence and θ=5.5°. (c) Magnetic field profiles ($|H_z|^2$) at z=60 μm and 90 μm.

Figure 4 shows the results of a FEM simulation of the designed non-periodic HCG structure. The simulated structure is the same as the one depicted in Fig. 2. The light source is a plane wave with a Gaussian power envelope and a wavelength of 1.55 μm. Its full width at half maximum (FWHM) is 30 μm. From Fig. 4(a) and 4(c), the deflection angle, θ is 5.5°, which is in good agreement with the value predicted by Eq. (1). In Fig. 4(b), the phase of the electric field, Φ(*x*) measured at z=10 μm matches well the desired phase profile. The slight deviation from the targeted linear phase profile can be attributed to the interference with the

diffracted near field: The transition from the near- to the far-field occurs around $z \sim d^2/\lambda = 25$ µm [9]. The total phase shift, ΔΦ measured in Fig. 4(b) is approximately 150° as designed in Fig. 3(b). These good agreements in θ and ΔΦ found between the RCWA-based periodic simulations and the FEM-based non-periodic simulations validate our assumption that local transmission phase is determined by local grating parameters.

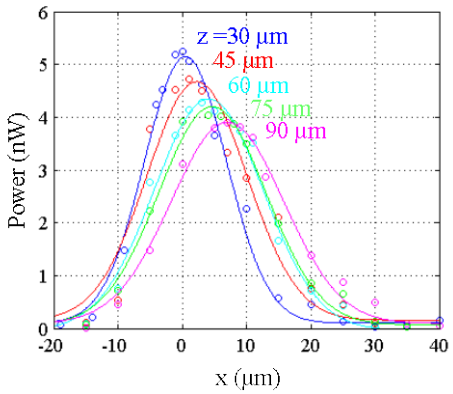

Fig. 5. Measured beam profiles at different distances from the HCG. Markers (hollow dots) are measurements and solid lines show corresponding fitted Gaussian profiles.

The non-periodic HCG with a linearly varying phase profile, simulated in Fig. 4, has been fabricated using the procedure outlined earlier. Using the setup described in Section 2, the power of the light transmitted through the grating is measured along the *x*-axis direction and at different distances, *z*, from the HCG. In order to avoid the complex transient fields from the near- to the far-field, it is measured from z=30 µm. The measurement results are presented in Fig. 5. The spatial position of the peak clearly shifts as the beam propagates further from the grating, indicating beam deflection. The measurements are fitted to a Gaussian distribution. The difference between the fitted curves and the measurements may have several explanations. First of all, due to beam steering, the beam profile would not be exactly Gaussian along the *x*-axis as the wave front would be tilted by an angle θ with respect to the *x*-axis. Furthermore, some uncertainty is introduced by the setup. The error in the position of the fibers was ±0.5 µm. From the Gaussian fits, the peak is displaced by ~7 µm from the first to the last measurements taken at a distance of 30 µm and 90 µm from the HCG, respectively. The measured steering angle is $\theta = \tan^{-1}[7/(90-30)] = 6.65° \pm 0.71°$. This value is in excellent agreement with the theoretical values for the considered grating design, including the prediction by Eq. (1).

5. Conclusions

We have demonstrated that high-index-contrast grating (HCG) reflectors can be used to manipulate the transmitted beam, while simultaneously maintaining high reflectivity for the incident beam. Fabricated structures with a non-periodic HCG region show a beam deflection of ~6°, in excellent agreement with numerical simulations. Basic design rules to realize gratings that impose an engineered phase front to the transmitted beam are explained and their applicability is demonstrated by comparison with simulation and characterization results. The ability of these HCGs to feature high reflectivity as well as wave front control can be advantageous for many applications, such as low cost laser fabrication. Furthermore, this approach can be generalized to obtain different phase profiles from the grating, broadening the set of possible applications as well as opening the possibility for integration of additional functionalities in compact and cheap devices.

Bibliography

[1] C. F. R. Mateus et al., "Broad-band mirror (1.12-1.62 μm) using a subwavelength grating", IEEE Photon. Tech. Lett. **16**, 1676 (2004).

[2] M.C.Y. Huang at al., "A surface-emitting laser incorporating a high-index-contrast subwavelength grating", Nat. Photon. **1**, 119-122 (2007).

[3] I.-S. Chung, J. Mørk, P. Gilet, and A. Chelnokov, "Subwavelength grating-mirror VCSEL with a thin oxide gap", IEEE Photon. Tech. Lett. **20**, 105 (2008).

[4] I.-S. Chung, et al., "Broadband MEMS-tunable high-index-contrast subwavelength grating long-wavelength VCSEL", IEEE J. Quant.Electron. **46**, 1245 (2010).

[5] I.-S. Chung and J. Mørk, "Silicon-photonics light source realized by III-V/Si-grating-mirror laser", Appl. Phys. Lett. **97**, 151113 (2010).

[6] D. Fattal et al., "Flat dielectric grating reflectors with focusing abilities", Nat. photon. **4**, 466-470 (2010).

[7] A.G. Baca and C.I.H. Ashby, "Fabrication of GaAs devices", The Institution of Engineering and Technology (2009), ISBN 978-1-84919-067-1.

[8] X. letartre et al., "Switching devices with spatial and spectral resolution combining photonic crystal and MOEMS structures", J. Lightwave Thechnol. **21**, 1691-1699 (2003).

[9] M. G. Moharam and T. K. Gaylord, "Rigorous coupled-wave analysis of planar-grating diffraction", J. Opt. Soc. Am. A **71**, 811-818 (1981).

[10] T. Tamir and H. C. Wang, "Scattering of electromagnetic waves by a sinusoidally stratified half-space: I. Formal solution and analysis approximations", Can. J. Phys. **44**, 2073-2094 (1966).

[11] M. G. Moharam et al., "Formulation for stable and efficient implementation of the rigorous coupled-wave analysis of binary gratings", J. Opt. Soc. Am. A **12**, 1068-1076 (1995).

[12] P. Lalanne and G. M. Morris, "Highly improved convergence of the coupled-wave method for TM polarization", J. Opt. Soc. Am. A **13**, 779-784 (1996).

[13] RODIS distribution and information are available at http://photonics.intec.ugent.be/research/facilities/design/rodis/default.htm

[14] ricwaa 1.0.2 distribution and information are available at http://www-personal.umich.edu/ zlei/

[15] T. Tamir et al., "Wave propagation in sinusoidally stratified dielectric media", IEEE Trans. Microwave Theory Tech. **MTT-12**, 323-335 (1964).

[16] O. C. Zienkiewicz and R. L. Taylor, "The Finite Element Method: Basic Formulation and Linear Problems", McGrow-Hill 6th ed. (2005) ISBN 0-7506-6320-0.

[17] Klaus-Jrgen Bathe, "Finite Element Method", John Wiley & Sons, Inc. (2007).

[18] O. C. Zienkiewicz, "The finite element method in engineering science", McGraw-Hill (1971).

[19] L. A. Coldren and S. W. Corzine, "Diode lasers and photonic integrated circuits", p. 438, Wiley, New York (1995).

[20] L. Carletti, R. Malureanu, J. Mørk and I.-S. Chung, "High-index-contrast grating reflector with steering ability for the transmitted beam", submitted to Opt. Express, the full text is available in Appendix.